ADVANCES IN ATMOSPHERIC SCIENCES, VOL. 40, JUNE 2023, 1021–1042

• **Original Paper** •

Predecessor Rain Events in the Yangtze River Delta Region Associated with South China Sea and Northwest Pacific Ocean (SCS-WNPO) Tropical Cyclones

Huiyan XU[1], Xiaofan LI[2], Jinfang YIN[3], and Dengrong ZHANG[*1]

[1]*Zhejiang Provincial Key Laboratory of Urban Wetlands and Regional Change*, *School of Information Science and Technology*, *Hangzhou Normal University*, *Hangzhou* 311121, *China*

[2]*Key Laboratory of Geoscience Big Data and Deep Resource of Zhejiang Province*, *School of Earth Sciences*, *Zhejiang University*, *Hangzhou* 310027, *China*

[3]*State Key Laboratory of Severe Weather (LaSW)*, *Chinese Academy of Meteorological Sciences (CAMS)*, *Beijing* 100081, *China*

(Received 10 March 2022; revised 1 October 2022; accepted 26 October 2022)

ABSTRACT

Predecessor rain events (PREs) in the Yangtze River Delta (YRD) region associated with the South China Sea and Northwest Pacific Ocean (SCS-WNPO) tropical cyclones (TCs) are investigated during the period from 2010 to 2019. Results indicate that approximately 10% of TCs making landfall in China produce PREs over the YRD region; however, they are seldom forecasted. PREs often occur over the YRD region when TCs begin to be active in the SCS-WNPO with westward paths, whilst the cold air is still existing or beginning to be present. PREs are more likely to peak in June and September. The distances between the PRE centers and the parent TC range from 900 to 1700 km. The median value of rain amounts and the median lifetime of PREs is approximately 200 mm and 24 h, respectively. Composite results suggest that PREs form in the equatorward jet-entrance region of the upper-level westerly jet (WJ), where a 925-hPa equivalent potential temperature ridge is located east of a 500-hPa trough. Deep moisture is transported from the TC vicinity to the remote PREs region. The ascent of this deep moist air in front of the 500-hPa trough and frontogenesis beneath the equatorward entrance region of the WJ is advantageous for the occurrence of PREs in the YRD region. The upper-level WJ may be affected by the subtropical high and westerly trough in the Northwest Pacific Ocean, and the occurrence of PREs may favor the maintenance of the upper-level WJ. The upper-level outflow of TCs in the SCS plays a secondary role.

Key words: tropical cyclone, heavy rain, westerly trough, upper-level jet stream

Citation: Xu, H. Y., X. F. Li, J. F. Yin, and D. R. Zhang, 2023: Predecessor rain events in the Yangtze River Delta region associated with South China Sea and Northwest Pacific Ocean (SCS-WNPO) tropical cyclones. *Adv. Atmos. Sci.*, **40**(6), 1021–1042, https://doi.org/10.1007/s00376-022-2069-3.

Article Highlights:

- Predecessor rain events in the Yangtze River Delta region related to the South China Sea and Northwest Pacific Ocean TCs are examined.
- PREs in the Yangtze River Delta region occur in the equatorward jet-entrance region of the upper-level westerly jet along the low-level baroclinic zone.
- Deep moisture from a tropical cyclone in the vicinity of a 500-hPa trough favors the occurrence of PREs in the Yangtze River Delta region.

1. Introduction

The Yangtze River Delta (YRD) region is located in the coastal region of Eastern China (Figs. 1a, b). Extending between 28°–33°N and 110°–124°E, it is one of the largest estuarine delta alluvial plains in China. Mid-latitude westerly troughs, regional lows, frontal cyclones, tropical cyclones (TCs), southwesterly monsoon, and terrain orographic forcing can induce torrential rainfall in the YRD region. The formation and development of heavy rainfall often involve multi-scale interactions between different factors under

* Corresponding author: Dengrong ZHANG
Email: zju_rs@126.com

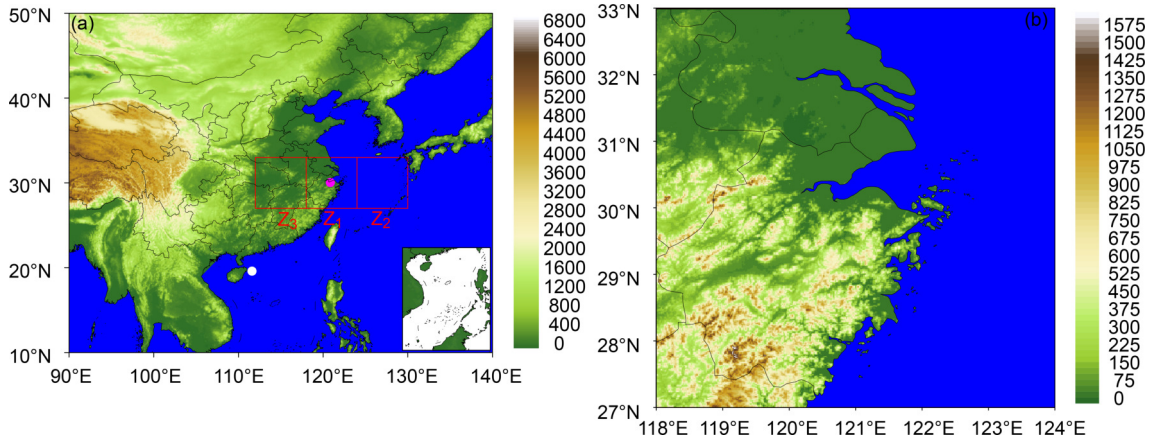

Fig. 1. Map of (a) East Asia, and (b) location and terrain (shaded, m MSL) of the Yangtze River Delta region in China denoted by Z_1. Boxes Z_2 and Z_3 are regions used in the trough detection method. Composite tropical cyclone (TC) locations are indicated by the solid white circle. The predecessor rain event (PRE) rainfall location is indicated by a solid magenta circle.

large-scale circulation conditions (Tao, 1980; Zhang et al., 2002; Xiong et al., 2003; Geng et al., 2004; Zhao et al., 2016; Cui et al., 2021; Liu et al., 2022a). TCs originating from the South China Sea or Northwest Pacific Ocean and approaching the YRD region have often caused heavy rainfall and severe disasters (Gao et al., 2009; Huang et al., 2014; Bao et al., 2015; Xu et al., 2021). The co-occurrence of TC and the astronomical high tide in coastal regions of China may cause severe floods and intrusion of seawater into cities, which may trigger secondary disasters (e.g., landslides, debris flows), causing severe economic losses and great social impacts (Liu et al., 2022b). For example, TC In-fa (2021) occurred coincidentally with the astronomical tide when making landfall in Zhoushan of Zhejiang province, and it caused floods in coastal regions (Huang et al., 2021). TCs can cause torrential rainfall directly when making landfall in coastal regions, and they may also cause heavy rainfall far away from the circulation center. Numerous studies have shown that TCs can produce heavy rainfall through interaction with a mid-latitude westerly trough over a region that may be far from the TC center (Pierce, 1939; Bosart and Carr, 1978). Cote (2007) and Chen (2007) proposed the term "predecessor rainfall event (PRE)" and "tropical cyclone remote precipitation (TRP)" to define confluent regions of torrential rainfall far away from a TC center, yet still closely associated with the TC. For example, the interaction of southeasterly flow and the outer circulation of Typhoon In-fa (2021) played a crucial role in causing the remote precipitation in Henan province on 19–21 July 2021 (Xu et al., 2022). The remote precipitation was extremely heavy with 818 mm in 48 hours and a maximum hourly rainfall of ~ 201.9 mm (Xu et al., 2022). The extreme rainfall caused severe economic losses and seven casualties, and the torrential rainfall flooded buildings and infrastructure and caused transportation, power, and communication disruptions (Cheng et al., 2022; Yin et al., 2022).

Considering the severe disasters caused by the inaccurate forecasting of PREs, many studies have investigated the causes of PREs around the world. Some researchers have detected PREs and examined the statistical characteristics of PREs; others have comprehensively examined a specified PRE case. Cote (2007) identified 47 PREs in the United States and found that PREs generally occur in the confluence zone well beneath the middle- and upper-level jet entrances in front of the mid-latitude trough, that moist tropical air is transported from the distant parent TC to this region, and that mesoscale surface boundaries actually trigger the PREs. Galarneau et al. (2010) further showed that frontogenetical forcing along a baroclinic zone can be important in producing PREs when deep moisture from a parent TC is present. Schumacher et al. (2011) revealed that removing TC-related deep moisture could reduce ~25% of the total precipitation amount by decreasing convective available potential energy (CAPE) in the inflow region of PREs. Moore et al. (2013) emphasized the relative locations of synoptic-scale flows and parent TCs in the occurrence of PREs to the east of the Rocky Mountains in association with Atlantic basin TCs.

PREs have also been studied in other areas where TCs frequently occur. Wang et al. (2009c) investigated the roles of TCs in PREs by inserting a bogus TC; their results show that remote precipitation can be enhanced when more moisture is transported to the PRE regions. Byun and Lee (2012) examined PREs over the Korean Peninsula through composite analyses and found that the northwestern synoptic-scale trough and the southeastern western Pacific subtropical high provide a favorable large-scale circulation background, with PREs occurring in a region beneath the upper-level jet entrance region with strong convective instability and quasi-geostrophic forcing. Cong et al. (2012) identified PREs in China during 1971–2006 and analyzed their mechanisms; their results indicate that the interactions among a westerly trough, the distant parent TC, and the location of the upper-level jet are dominant in determining the occurrence and development of PREs. Ding et al. (2017) examined PREs during 2000–09 in China and summarized four synoptic modes by analyzing the relationships among TCs, subtropical

highs, and PREs; the results show that these interactions are important in determining rain amounts in the PRE region.

Physical processes responsible for the torrential rainfall have also been investigated. Nava (2016) examined cloud radiative processes in PREs and showed that cloud-radiative feedback (CRF), the interaction of hydrometeor species with shortwave and longwave radiation can ultimately result in more precipitation by producing a more robust PREs structure with strong convective activity. Yuan et al. (2018) examined PREs in China's low-latitude highlands in relation to Bay of Bengal TCs and found that the PREs occurred beneath the equatorward entrance region of the upper-level East Asia subtropical jet in the presence of abundant moisture conveyed from Bay of Bengal TCs and enhanced frontogenesis due to the interaction between the TCs and mid-latitude troughs.

Besides these frequently occurring regions, predecessor rainfall events (PREs) associated with TCs and mid-latitude weather systems can also occur in the YRD region (Duan et al., 2020; He et al., 2020; Chen et al., 2021). Numerous studies have examined the large-scale synoptic conditions, thermal, dynamics, and microphysical processes associated with TCs that have made landfall in these coastal areas (Kueh et al., 2009; Wang et al., 2009a, b, 2010; Lee and Choi, 2010; Huang et al., 2011, 2014; Van Nguyen and Chen, 2011; Chien, 2014; Xu, 2015; Xu et al., 2017). However, little attention has been paid to YRD PREs associated with the South China Sea and Northwest Pacific Ocean (SCS-WNPO) TCs, despite the fact that PREs in the YRD region associated with SCS-WNPO TCs have wrought havoc in coastal cities, and the associated rainfall amounts have often been under-predicted or not forecasted at all (Luo, 2018; He et al., 2020; Chen et al., 2021).

The inability of numerical models to accurately forecast the interaction of mid-latitude weather systems and TCs, and the insufficient attention operational forecasters give to PREs, can lead to a lack of adequate preparation with regard to PRE occurrence, and subsequently to occasional disastrous effects. Consequently, consideration must be given to the potential for extreme rainfall in the confluent region well in advance of the possible occurrence of heavy parent TC rainfall associated with the tropical system to the south.

This study will mainly focus on the effects of large-scale circulation and the remote effects of SCS-WNPO TCs on heavy rainfall related to PREs in the YRD region. PREs with TCs and non-predecessor rain events with TCs are separately examined to investigate the remote effects of SCS-WNPO TCs on PREs in the YRD region. The aims of this study are (1) to examine the climatology of PREs in the YRD region associated with SCS-WNPO TCs, and (2) to investigate possible mechanisms for PREs over the YRD region.

This paper is organized as follows. The datasets and methodology are described in Section 2. In section 3, the climatology of PREs and the statistical analysis of the relationship between SCS-WNPO TCs and PREs over the YRD region are presented. A composite analysis of the synoptic circulations and possible factors favorable for the development of PREs over the YRD region is shown in section 4. Finally, the conclusions and further discussion are provided in section 5.

2. Data and methodology

2.1. *Datasets*

The precipitation datasets used to detect PREs cover the period from 2010 to 2019. Climate Prediction Center Morphing technique (CMORPH) was developed by the National Oceanic and Atmospheric Administration (NOAA) Climate Prediction Center (CPC) in the United States, and it was used to produce global precipitation analyses with approximately 8 km spatial resolution every 30 min using estimates determined from passive microwave and infrared data with high temporal and spatial resolution (Joyce et al., 2004; Xie et al., 2013, 2017). CMORPH Version 1.0 rainfall products verified in different regions (Sun et al., 2016; Xie et al., 2017, Liu et al., 2019) have generally shown good agreement with rain gauge observations. The China Meteorological Administration 0.1° × 0.1° hourly rain products (CMA, 2011) were obtained using land-based precipitation measurements from over 3000 weather stations to correct the CMORPH precipitation estimates from NOAA CPC (Joyce et al., 2004; Shen et al., 2013).

Additionally, best track data and reanalysis data were used in this study. The Regional Specialized Meteorological Center (RSMC) Tokyo-Typhoon Center affiliated with the Japanese Meteorological Agency (JMA, 2014) provided the historical best track data for TCs in the SCS-WNPO. The RSMC best track datasets contain TC locations and intensities over the SCS-WNPO, with an interval of generally 6 h. The intensity datasets of TC are from Japan Meteorological Agency available at: https://www.data.jma.go.jp/multi/cyclone/cyclone_caplink.html?lang=en. The TC locations were obtained by extracting latitude and longitude data along the lines of the best track data. Since there is no detailed information about whether a TC made landfall in China or not in the JMA TC dataset, the TC datasets from CMA were used, namely, detailed information for the tropical cyclones making landfall in China was obtained from CMA Tropical Cyclone Data Center for the Western North Pacific Basin (Ying et al., 2014; Lu et al., 2021; available at https://tcdata.typhoon.org.cn). Geopotential height at 200 hPa, 500hPa, and 850 hPa, surface pressure, upper-level winds at 200 hPa, relative humidity, and air temperature from reanalysis datasets were used for the composite analysis of the atmospheric environments. Orography data used in this study was based on Earth topography five-minute grid (ETOPO5) data (Data Announcement 88-MGG-02: Digital relief of the Surface of the Earth; NOAA, National Geophysical Data Center, Boulder, Colorado, 1988).

2.2. *Identification of PREs*

Following Cote (2007), Chen (2007), Ding et al. (2017),

and Yuan et al. (2018), deep moisture from the vicinity of the TC, coherent rainfall far away from the TC, and the existence of a mid-latitude trough were all considered to determine the PREs. Specifically, PREs were identified by the following criteria: (1) a coherent area of rainfall persisting for at least 12 h in the YRD region, and which was spatially separated from the rainfall area directly associated with the TC; (2) at least 12 hours of rainfall greater than 30 mm (CSN, GB/T 28592–2012) for at least 4 grid points in the YRD region, and 12 hours of rainfall more than 5 mm for at least 20 grid points surrounding the above 4 grid points; (3) deep tropical moisture transported from the TC vicinity to the YRD region forming a moisture channel with a water vapor flux at 850 hPa $\geqslant$ 5 g (s hPa cm)$^{-1}$, and total-column precipitable water > 40 mm as in Cote (2007), Galarneau et al. (2010), Schumacher et al. (2011), and Moore et al. (2013); (4) the existence of a mid-latitude trough in the YRD region. Following the trough detection scheme applied by Herrera et al. (2001) and Knippertz (2004), a parameter larger than 10.0 gpm was used to detect a trough using 6-hourly National Center for Environmental Prediction (NCEP) global forecast system final (FNL) operational global analysis data with a horizontal resolution of 1°×1°. The parameter was defined as the difference between the averaged 500-hPa geopotential heights over the YRD region (red rectangular area marked as Z1 in Fig.1a) and the mean geopotential heights over the west and east surrounding rectangular areas (marked as Z2 and Z3) at the same latitudes. The detected trough was further checked by plotting 500hPa geopotential height and winds, and surface winds.

The Hybrid Single-Particle Lagrangian Integrated Trajectory (HYSPLIT) model (version 5.1) was also applied for each PRE candidate to verify whether the air parcels originated from the parent TC vicinity. The backward air parcel trajectories were tracked using the HYSPLIT model and NCEP Global Data Assimilation System (GDAS1) Archive processed by NOAA's Air Resources Laboratory (ARL) with NCEP's 1-degree GRIB output (the HYSPLIT model and the GDAS1 datasets can be downloaded at: http://ready.arl.noaa.gov/HYSPLIT.php). The HYSPLIT model uses meteorological data (e.g., horizontal wind components, temperature, height, pressure, or rainfall fields) in diagnostic case studies or climatological analyses. It is a kind of Lagrangian model in which the advection and diffusion components are calculated independently (Draxler and Hess, 1998). If the air particles originated from the TC vicinity, and met the other PRE criteria, then the YRD rainfall event was considered a PRE. Those cases with a TC that passed through the domain of 19°–21°N and 111°–113°E and did not generate heavy rainfall in the YRD region during the period in a TC' s lifetime were denoted as NPREs. Detailed descriptions for the selection of NPREs are shown in section 3.

2.3. *Composite analysis*

A composite analysis is a useful method for exploring the basic characteristics of a meteorological phenomenon (e.g. a tropical cyclone) by collecting a large number of cases. Those cases can be used to conduct composite analysis by a specific meteorological factor to retain a common character, which may not include the specific character of an individual case. The composite analysis generally calculates the composite mean or other statistical quantity, which highlighted the predominant signatures that appeared repeatedly in the tropical cyclone cases. The composite results can show how the factors used in the composite analysis affect the meteorological phenomenon. Composite analysis has been used in the TC research for decades (Frank, 1977; McBride and Zehr, 1981; Pfeffer and Challa, 1981; Hanley et al., 2001; Galarneau et al., 2010; Byun and Lee, 2012; Moore et al., 2013; Ding et al., 2017; Yuan et al., 2018). It has proven to be effective in investigating favorable synoptic environments for the development of TC-related heavy rainfall. In this study, to understand the favorable environments for the development of PREs in the YRD region, the differences and similarities in synoptic environments between PREs and NPREs were compared by applying a composite analysis.

The frontogenesis function was first proposed by Petterssen (1936) and later formulated by Petterssen (1956), Palmen and Newton (1969), and Ninomiya (1984), as a useful diagnoistic tool now widely used in weather analysis. Following Yuan et al. (2018), the two-dimensional horizontal frontogenesis function was computed using the NCEP FNL reanalysis data. Frontogenesis was computed to determine its role in triggering vertical motion and promoting heavy rainfall in the YRD region. Additionally, the frontogenesis was calculated as the local change for the magnitude of the horizontal equivalent potential temperature gradient.

Following Ninomiya (1984), frontogenesis (FG) is expressed by

$$\mathrm{FG} = \frac{\mathrm{d}|\nabla\theta_e|}{\mathrm{d}t}, \tag{1}$$

where θ_e is the equivalent potential temperature. $\nabla\theta_e$ denotes the horizontal gradient of equivalent potential temperature and FG represents the Lagrangian change of the equivalent potential temperature gradient.

Following Hoskins et al. (1985), and Hanley et al. (2001), and the corrected PV equation (refer to page 264, Eq. 4.5.93) in Bluestein (1992), the representation of the potential vorticity (PV) in pressure coordinate can be given by

$$\mathrm{PV} = -g\left[\left(\zeta_p + \boldsymbol{f}\right)\frac{\partial\theta}{\partial p} + \boldsymbol{k}\cdot\left(\frac{\partial \boldsymbol{V}}{\partial p}\times\nabla_p\theta\right)\right], \tag{2}$$

$$f = 2\Omega\sin\Phi, \tag{2.1}$$

where the first term ζ_p is the vertical component of relative vorticity, and $\boldsymbol{V}$ is the horizontal wind vector. f is coriolis parameter, Ω is the rotation vector of the earth about its axis at the rate of 2π radians every sidereal day (7.292×10^{-5} s^{-1}), and Φ is the latitude. ∇_p is the three-dimentional gradient operator in xyp space. θ is the potential tempera-

ture. k is a unit vertical vector. The potential vorticity (PV) is usually expressed in potential vorticity units, written as PVU (1PVU = 1×10^{-6} m^2 K s^{-1} kg^{-1}). More detailed information about this equation can be found in Hoskins et al. (1985).

3. PRE statistics during 2010–19

Predecessor rainfall events associated with SCS-WNPO TCs can occur in China, and most of these cases occurred in regions surrounding the Bohai sea (Cong et al., 2012). Those which occurred in the YRD region were often poorly predicted (Duan et al., 2020; Chen et al., 2021). A total of 252 TCs occurred in the SCS-WNPO region during 2010–19 according to RSMC best track dataset. Of these, a total of 58 predecessor rainfall events associated with SCS-WNPO TCs occurred in China 2019, accounting for 23.0% of the total SCS-WNPO TCs. Among these PREs, a total of 12 PREs (Table 1) occurred in the YRD region (PRE-related TCs). Considering that a total of 9 TCs made landfall in the YRD region during 2010–19 (Ying et al., 2014; Lu et al., 2021), the number of PREs is not negligible. A total of 17 TCs related to NPREs (NPRE-related TCs) were detected.

Figure 2 shows monthly distributions of frequency for all 252 SCS-WNPO TCs, 12 PRE-related TCs, and 17 NPRE-related TCs. This shows that PRE-related and NPRE-related TCs can occur from June to October over the YRD region. Approximately 20 TCs (7.9%) and 50 TCs (19.8%) of these 252 SCS-WNPO TCs occurred in June and September, respectively. By comparison, nearly 25.0% and 41.7% of these PRE-related TCs occurred in June and September, respectively (Fig. 2). The results indicate that PRE-related TCs preferentially occur in June and September. Of these 252 SCS-WNPO TCs, nearly 73 TCs (29.0%) made landfall in China during 2010–19 (Ying et al., 2014; Lu et al., 2021). Seven of these 73 landfall TCs (nearly 10%) produced PREs over the YRD region.

It is apparent from Fig. 3 that of all the 252 SCS-WNPO TCs during 2010–19, approximately 55 TCs (21.8%) fell into the category of a tropical storm, and 168 TCs (66.6%) reached at least the category of a typhoon. Of all the NPRE-related TCs without heavy rainfall over the YRD region, approximately 33.3% were associated with tropical storms and 46.7% were related to typhoons. Of all the PRE-related TCs, approximately 33.3% were associated with tropical storms, and 50% were related to TCs that reach the category of typhoon. This suggests that the frequency distribution of NPRE-related TCs without heavy rainfall and that of PRE-related TCs with heavy rainfall over the YRD region are quite similar, and they are generally different from that of all SCS-WNPO TCs. This analysis further indicates that PREs over the YRD region are more likely associated with TCs categorized as typhoons, although SCS-WNPO TCs in weaker categories also probably produce PREs over the YRD region.

Figure 4 shows the tracks of TCs that produced predecessor rainfall events and the spatial distribution of TC location frequency. For simplicity, a TC that contained a period when it moved northward while active in the WNPO was classified as a northward moving TC, and the remaining TCs moved northwestward to the SCS were classified into northwestward moving TCs. The 75% of the TCs associated with PREs over the YRD region including northwesterly tracks passed through the South China Sea (SCS); the remaining 25% of TCs included northerly tracks into high latitudes in the Northwest Pacific Ocean (WNPO). The spatial distribution of TC location frequency reveals that PRE-related TCs occur most frequently on the southeast of Hainan Island and southwest of Taiwan Island, with a frequency of 5 and 6, respectively. The mean location of northwestward moving TCs was generally included in the area of 19°–21°N and 111°–113°E, denoted by a small red rectangle in Fig. 4. The

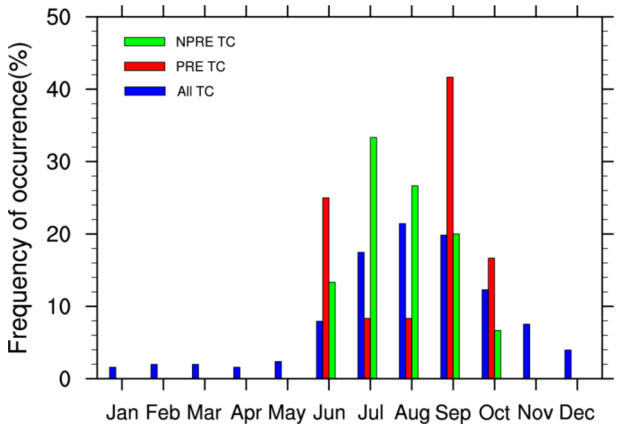

Fig. 2. Monthly frequency distributions of all tropical cyclones (TCs) in the Northwest Pacific Ocean and South China Sea (blue bars), TCs that produced predecessor rain events (PREs; red bars), and TCs without heavy rainfall (green bars) over the Yangtze River Delta region of China during 2009–19.

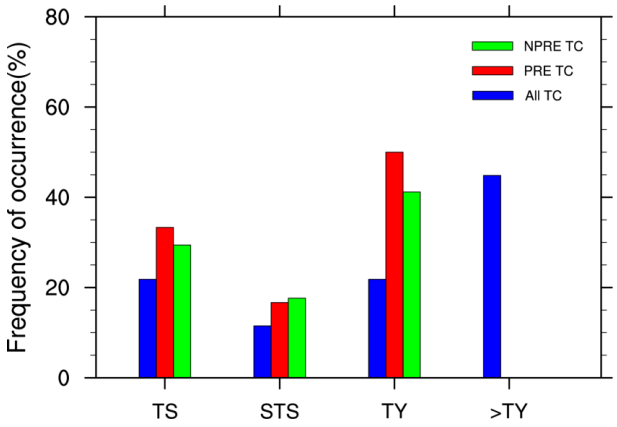

Fig. 3. Frequency distributions of maximum tropical cyclone (TC) intensity of all TCs in the Northwest Pacific Ocean and South China Sea (blue bars), TCs that produced predecessor rain events (PREs; red bars), and TCs without heavy rainfall (green bars) over the Yangtze River Delta region of China during 2009–19. TS, STS, and TY denotes tropical storm, severe tropical storm, and typhoon, respectively.

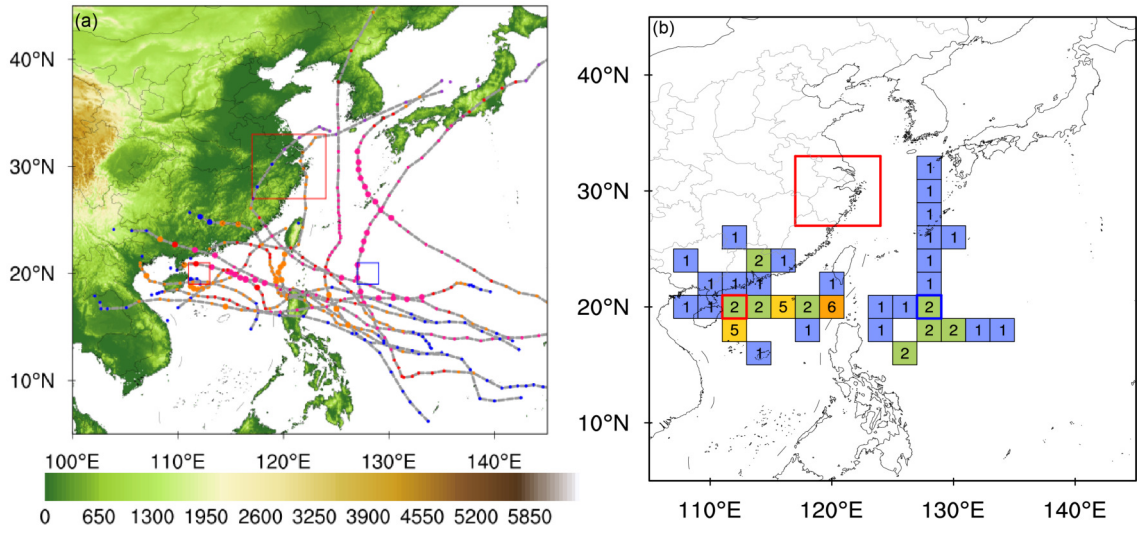

Fig. 4. (a) Tracks of tropical cyclones (lines with colored dots) and terrain height (shaded) that produced predecessor rainfall events and (b) spatial distribution of TC location frequency in each 2° × 2° grid box at the time when PREs occurred in the Yangtze River Delta region. Color dots mark the tropical cyclone (TC) positions every 6 h, and different colors denote different intensity categories for a TC (Blue: TD, dark orange: TS, red: STS, deep pink: TY, dark orchid: Extra-tropical Cyclone). Larger color dots at the track represent the times of the track when a TC produced PREs in the YRD region. The small red rectangle denotes the area (generally 19°–21°N,111°–113°E) where the mean location of all the northwestward moving PRE-related TCs. The small blue rectangle denotes the area (generally 19°–21°N,127°–129°E) where the mean location of all the northward moving PRE-related TCs. The large red rectangle denotes the YRD region (generally 27°–33°N,118°–124°E).

mean location of northward moving TCs was generally included in the area of 19°–21°N and 127°–129°E, denoted by a small blue rectangle in Fig. 4. The location frequency of the PRE-related SCS TCs was 2 over the PRE-related WNPO TCs.

To examine the impact of TC location on PREs in the YRD region, we separated the TCs reaching the category of tropical storm intensity or higher into those passing through the domain of 19°–21°N and 111°–113°E in the SCS without heavy rainfall (NPRE) and those passing through the domain of 19°–21°N and 127°–129°E in the WNPO without heavy rainfall in the YRD region (NPRE_NE). Figure 5 shows the composite surface rainfall for PRE cases, NPRE cases, and NPRE_NE cases. PRE-related heavy rainfall shows southwest and northeast orientation, with a maximum value of mean surface rainfall of 114.1 mm; the maximum rainfall center was in the Bay of Hangzhou (30.05°N, 120.85°E; denoted by as A). PRE-related TCs were located to the southeast of Hainan Island, where heavy rainfall may be associated with the TC circulation (rainfall center B1). Heavy rainfall in the eastern Philippines may be attributed to the northward moving TCs (center C). For NPRE cases, heavy rainfall mainly occurred to the southeast of Hainan (B1). However, for NPRE_NE cases, heavy rainfall only occurred to the east of the Philippines (C). This suggests that the northwestward tracking TCs may be related to heavy rainfall to the southeast of Hainan (B1); however, they cannot guarantee the formation of heavy rainfall in the YRD region.

Figure 6 shows box-and-whisker diagrams of PRE lifetime (hours), percentage of PRE heavy rainfall coverage (12 h rainfall of ⩾ 30 mm), maximum PRE rainfall (mm), and distance between the TCs and PRE rainfall regions when the PRE occurred in the YRD region. PRE centers were defined as the location of the maximum heavy rainfall of each PRE in the YRD region. The medium PRE lifetime was 24 h, with the shortest and longest times of 18 h and 36 h, respectively (Fig. 6a). The areal extent of heavy rainfall associated with PREs was defined as the percentage of grids experiencing heavy rainfall (⩾ 30 mm rainfall in 12 h). The median areal extent of heavy rainfall was approximately 13.5%, ranging from 2% to 22% for the 25th and 75th percentiles, respectively (Fig. 6b). The maximum rainfall of PREs ranged from 62.5 to 566.9 mm, with a median value of 201 mm, and 25th and 75th percentile maximum rainfall of 100 and 380 mm, respectively (Fig. 6c). The distances between PREs and parent TCs ranged from 889.1 to 1730.4 km, with a median value of 1387.5 km, and 25th and 75th percentile distances of 1300 and 1600 km, respectively (Fig. 6d).

4. Synoptic-scale environments for PREs

To examine favorable environments for the formation of PREs in the YRD region, we compared the synoptic environments of PREs with those of NPRE cases. To examine if TCs passing the area of 19°–21°N and 127°–129°E (northward moving TCs) located to the east of the Philippines, play roles in generating heavy rainfall in the YRD region, the composites of atmospheric environments for NPRE_NE

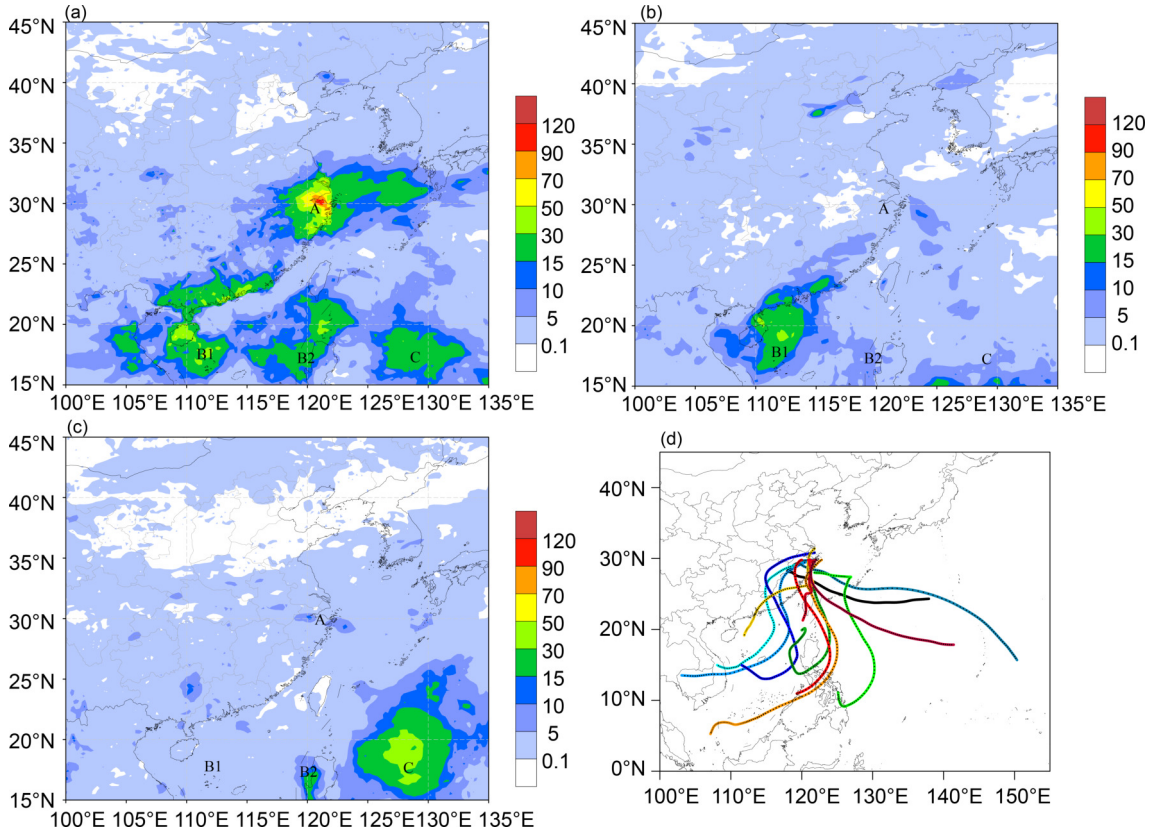

Fig. 5. Composite of mean surface rainfall (shaded, mm) for (a) predecessor rain event (PRE) cases, (b) northwestward moving TCs passing through the domain of 19°–21°N and 111°–113°E but not associated with heavy rainfall in the YRD region (NPRE cases), (c) northward moving TCs passing through the domain of 19°– 21°N and 127°–129°E but not associated with heavy rainfall in the YRD region (NPRE_NE cases), (d) backward trajectories for air parcels originated from the SCS-WNPO TCs vicinity, generated by tracking the backward trajectory using HYSPLIT model for each PRE case.

cases were also investigated. Composites of the synoptic environments for PRE cases, NPRE cases, and NPRE_NE cases were generated using NCEP FNL 6-hourly data. Specifically, the composite of synoptic environmental fields for PRE, NPRE, and NPRE_NE cases were obtained by taking the average of the 6-hourly atmospheric environments using the 6-hourly NCEP FNL data during the whole lifetime of the PRE, NPRE, and NPRE_NE cases, respectively.

Backward air parcel trajectories indicate that air particles in the YRD region can be traced to the SCS and WNPO regions (Fig. 5d), and one of the major mean TC locations was to the southeast of Hainan Island when TCs generated PREs in the YRD region. Present were anomalously low 500 hPa geopotential heights over Hainan Island for both PRE and NPRE cases, whilst mid-latitude circulations differed for each kind of case. The Pacific subtropical high expanded from the Northwest Pacific to the East China Sea, and the western-expanding point of the subtropical high extended more westward for NPRE cases than that for PREs (Figs. 7a, 7b). In the mid-latitudes, there was a westerly trough located over East China for PRE cases (Fig. 7a). A two-sided student's *t*-test for the PREs and the weighted monthly long-term (2010–19) climatology suggested that the anomalous 500hPa geopotential heights for the PREs in the YRD region was statistically significant at the 95% level (Fig. 7d). Although the circulation was generally straight over the East China for NPRE cases (Fig. 8b), a student's *t*-test showed that the 500hPa geopotential heights between PREs and NPRE cases were significantly different in the PRE regions (Fig. 7e). Associated with the distributions of 500 hPa geopotential height fields, southwesterly winds in the eastern TCs transported warm, humid air to the YRD region for PRE cases (Fig. 7a, Fig. 8a). A two-sided student's *t*-test for the PREs and the weighted monthly long-term (2010–19) climatology suggested that the meridional wind components of the PREs in the YRD region were statistically significant at the 95% level (Fig. 8d). Southwesterly winds were much weaker for NPRE cases (Fig. 8b, Fig. 9b). A student's *t*-test showed that the difference of 700hPa meridional winds between PREs and NPRE cases was statistically significant at the 95% level in the SCS and PRE regions (Fig. 8e). Correspondingly, the vertical velocity at 500 hPa was less than −0.5 Pa s^{-1} in the YRD region for PRE cases in response to upward motions over the YRD region (Fig. 7a, Fig. 8a); while no upward motions occurred over the YRD region for NPRE cases (Fig. 7b, Fig. 8b).

The Pacific subtropical high expanded from the Northwest Pacific to the East China Sea, and the western-expanding

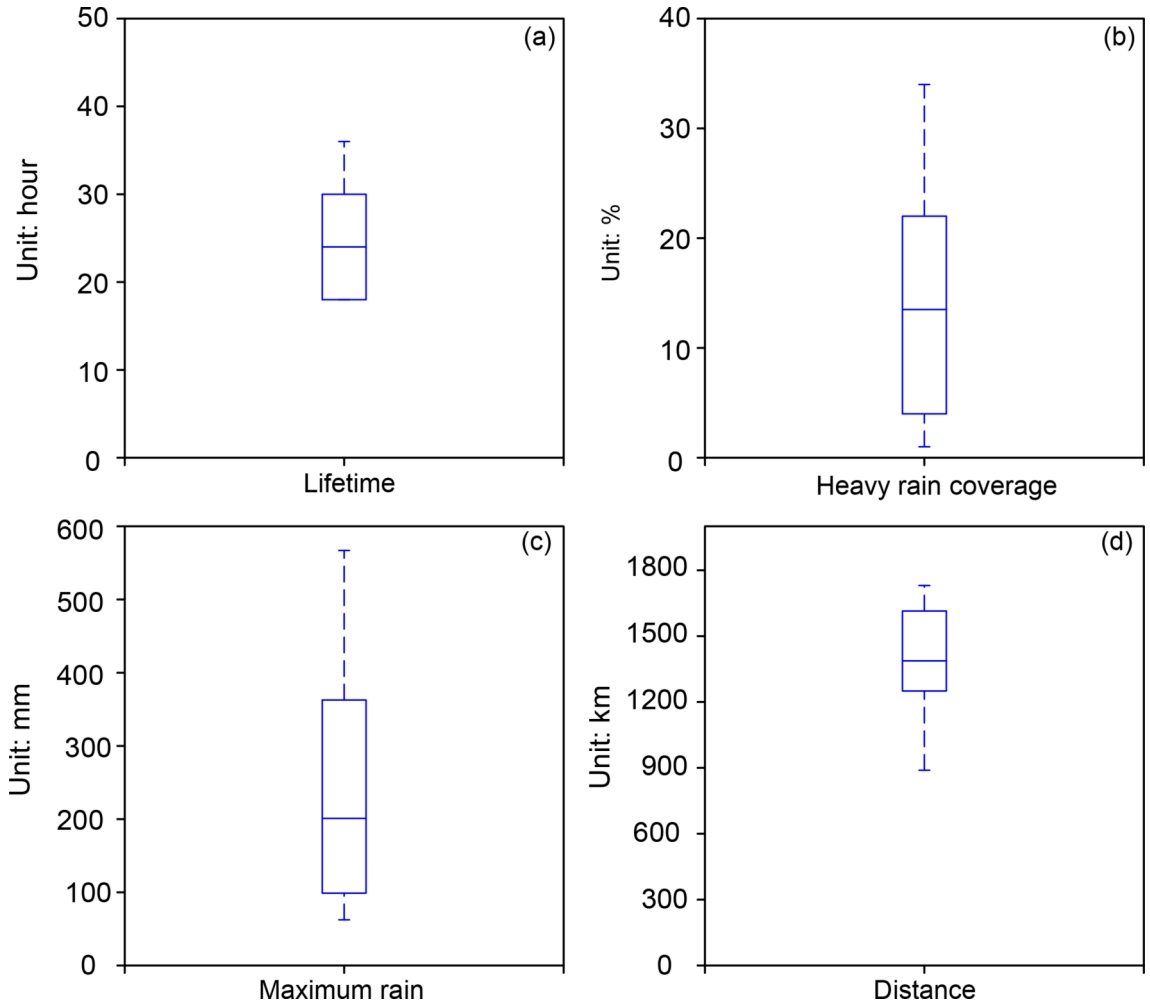

Fig. 6. Box-and-whisker diagrams of (a) predecessor rain event (PRE) lifetime (hours), (b) the percentage PRE areal extent during heavy rainfall (12 h rainfall ⩾ 30 mm), (c) maximum accumulated rainfall of PRE (mm), and (d) distance between the tropical cyclone (TC) and the rainfall region for PREs in the Yangtze River Delta region of China. The upper (lower) bound of the box marks the 75th (25th) percentile, and the symbol "—" indicates the median value. Whiskers mark the minimum and maximum values.

point of the subtropical high reached 135°E for NPRE_NE cases (Fig. 7c). For NPRE_NE cases, there was a mid-latitude trough located over the YRD region for TCs passing 19°–21°N and 127°–129°E (east of the Philippines). A student's *t*-test showed that the 500hPa geopotential heights between NPRE_NE and NPRE cases were significantly different in the SCS and PRE regions (Fig. 7f). There were northeasterly wind anomalies along the southeast coast of China, indicating the moisture from SCS to the YRD region was reduced. The deficiency of water vapor condition was unfavorable for the occurrence of heavy rainfall over the YRD region for NPRE_NE cases (Fig. 7c, Fig. 8c). A student's *t*-test showed that the 700hPa meridional winds between NPRE_NE and NPRE cases were significantly different in the SCS and YRD regions (Fig. 8f). Correspondingly, no upward motions occurred over the YRD region for NPRE_NE cases (Fig. 7c, Fig. 8c). This above analysis indicates that neither the existence of TCs in the region of 19°–21°N and 127°–129°E, nor the mid-latitude trough over the YRD region alone is sufficient to cause heavy rainfall in the YRD region.

The above analysis shows that a 500-hPa westerly trough was located in the YRD region, the Western North Pacific subtropical high expanded to the East China Sea, and that such configuration of atmospheric circulation may be important for the occurrence of PREs. It has been previously pointed out that the combined approach of the low-pressure system over land and the Western North Pacific subtropical high is beneficial to the reinforcement of the pressure gradient force, which favors strengthening of the local southwesterly wind (Chang et al., 2000; Zhang et al., 2000; Zhao et al., 2003, 2007).

Also as a consequence of the approaching westerly trough and Western North Pacific subtropical high, the strengthening pressure gradient may be favorable to enhance transport of tropical moisture into the YRD region. The enhanced transport of tropical moisture to the YRD region is further presented by additional analyses. Figure 9a

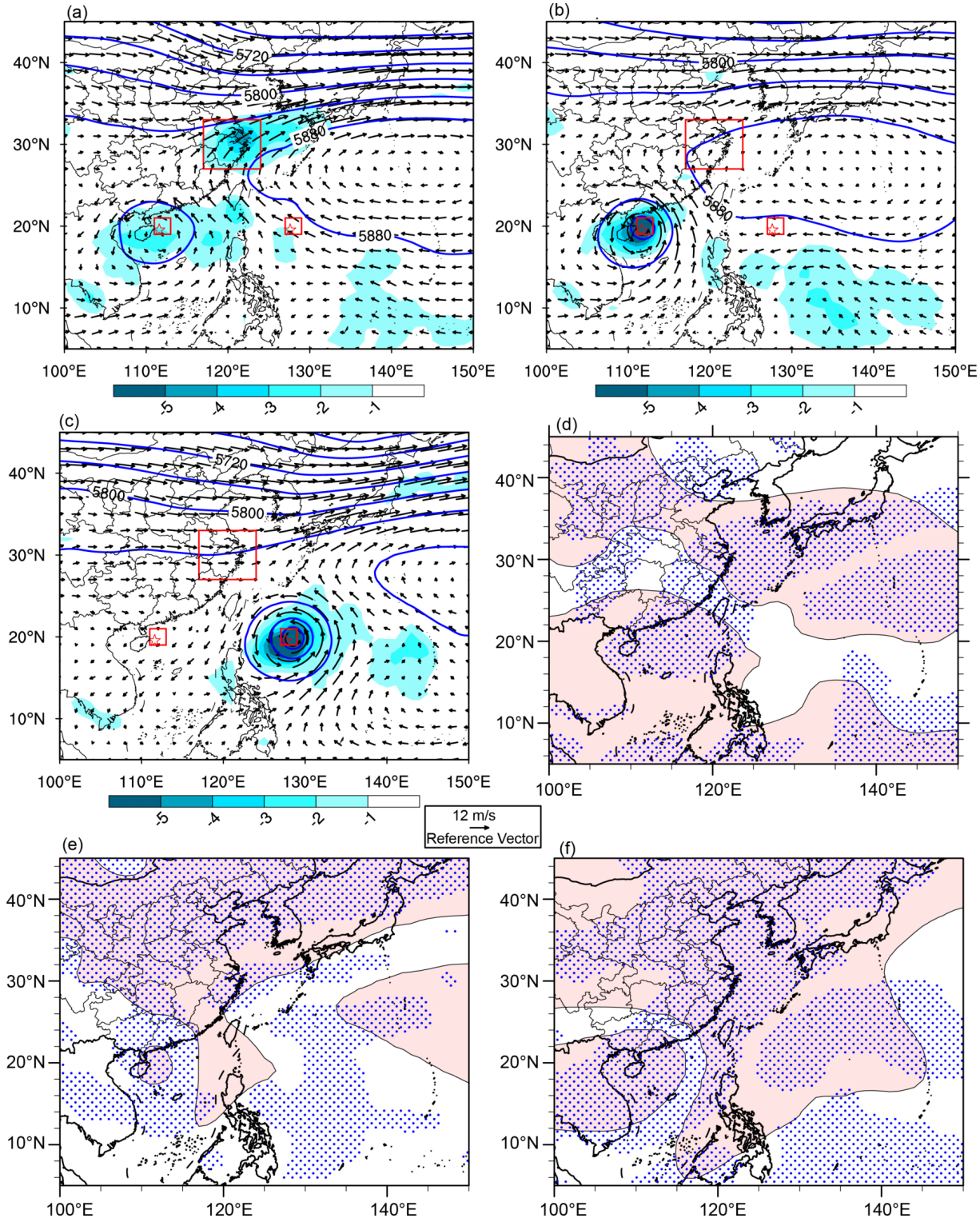

Fig. 7. Composite 500 hPa geopotential height (solid line, gpm) for (a) predecessor rain event (PRE) cases, (b) northwestward moving TCs passing through the domain of 19°–21°N and 111°–113°E but not associated with heavy rainfall in the YRD region (NPRE cases), and (c) northward moving TCs passing through the domain of 19°–21°N and 127°–129°E but not associated with heavy rainfall in the YRD region (NPRE_NE cases); (d) the significant *t*-test of the difference between PRE and the weighted monthly long-term (2010–19) climatology for 500 hPa geopotential heights and precipitable water; and the significant *t*-test of the difference between (e) PRE and NPRE cases, and (f) NPRE_NE and NPRE cases. Blue dots (red shaded) denote the difference in total precipitable water (500 hPa geopotential height) in panels (d), (e), and (f). Composite tropical cyclone (TC) locations are indicated by pentagrams. Shading in panels (a) , (b), and (c) indicates vertical velocity at 500 hPa (units: 10^{-1} Pa s^{-1}). The rectangles denote the same regions as in Fig. 4.

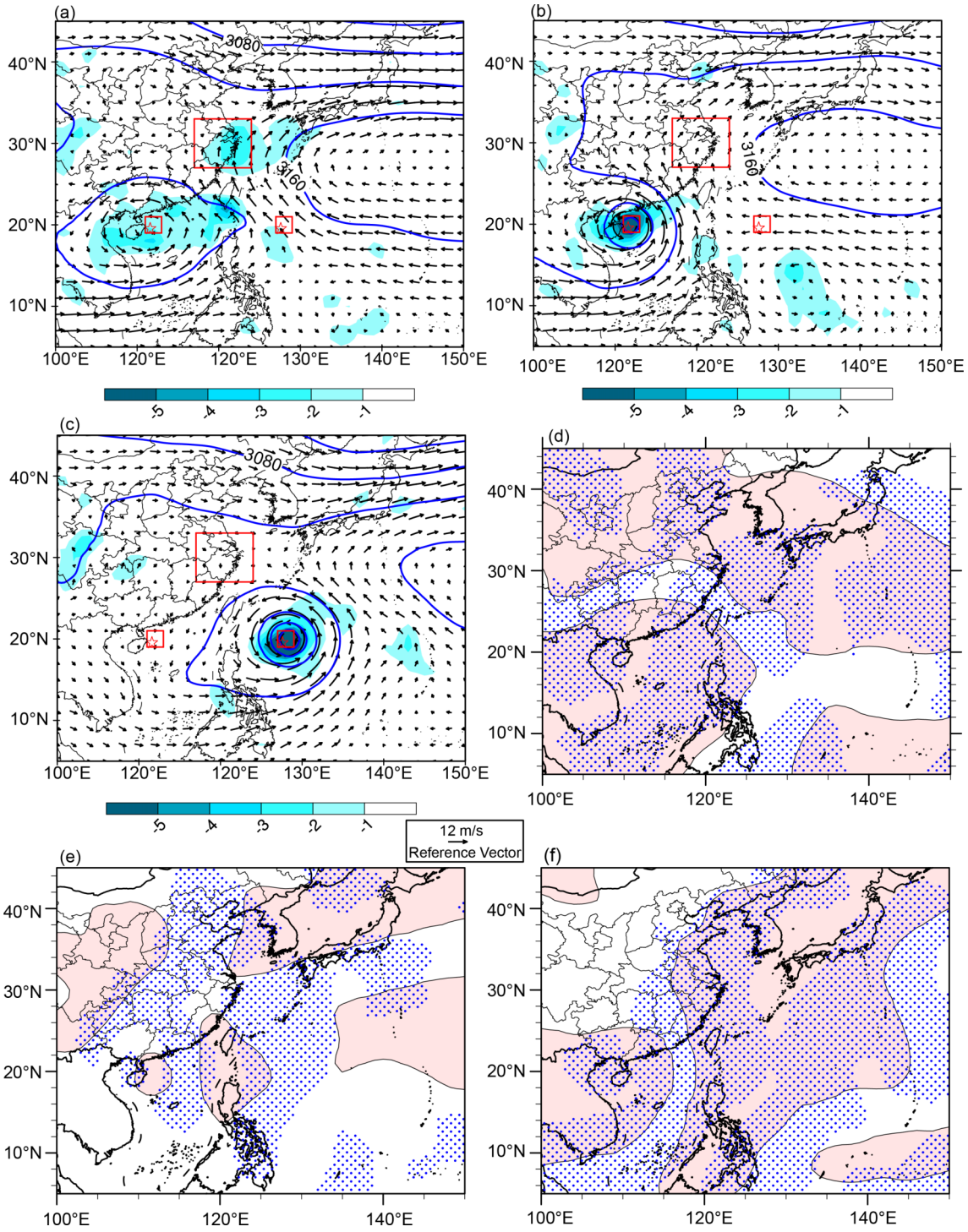

Fig. 8. As in Fig. 7, except for composite 700 hPa geopotential height (solid lines, gpm). Shading indicates vertical velocity at 700 hPa (units: 10^{-1} Pa s^{-1}).

shows that the precipitable water is greater than 50 mm in the environment of PREs in the YRD region, thus indicating that water vapor content was abundant in the YRD region. A two-sided student's *t*-test for the PREs and the weighted monthly long-term (2010–19) climatology suggested that the total precipitable water (TPW) of the PREs in the YRD region was statistically significant at the 95% level (Fig. 9d). Water vapor was transported from the TC vicinity to the YRD region by southwesterly flow with a column-integrated water vapor flux exceeding 300 kg m^{-1} s^{-1}. This is also generally true for the NPRE cases, for which the tropical moisture is transported by southwesterly winds from east of the TCs to the YRD region, with a column-integrated water vapor flux of nearly 300 kg m^{-1} s^{-1} and precipitable water of ~50 mm (Fig. 9b) in the YRD region. A student's *t*-test showed that the TPW between PREs and NPRE cases were

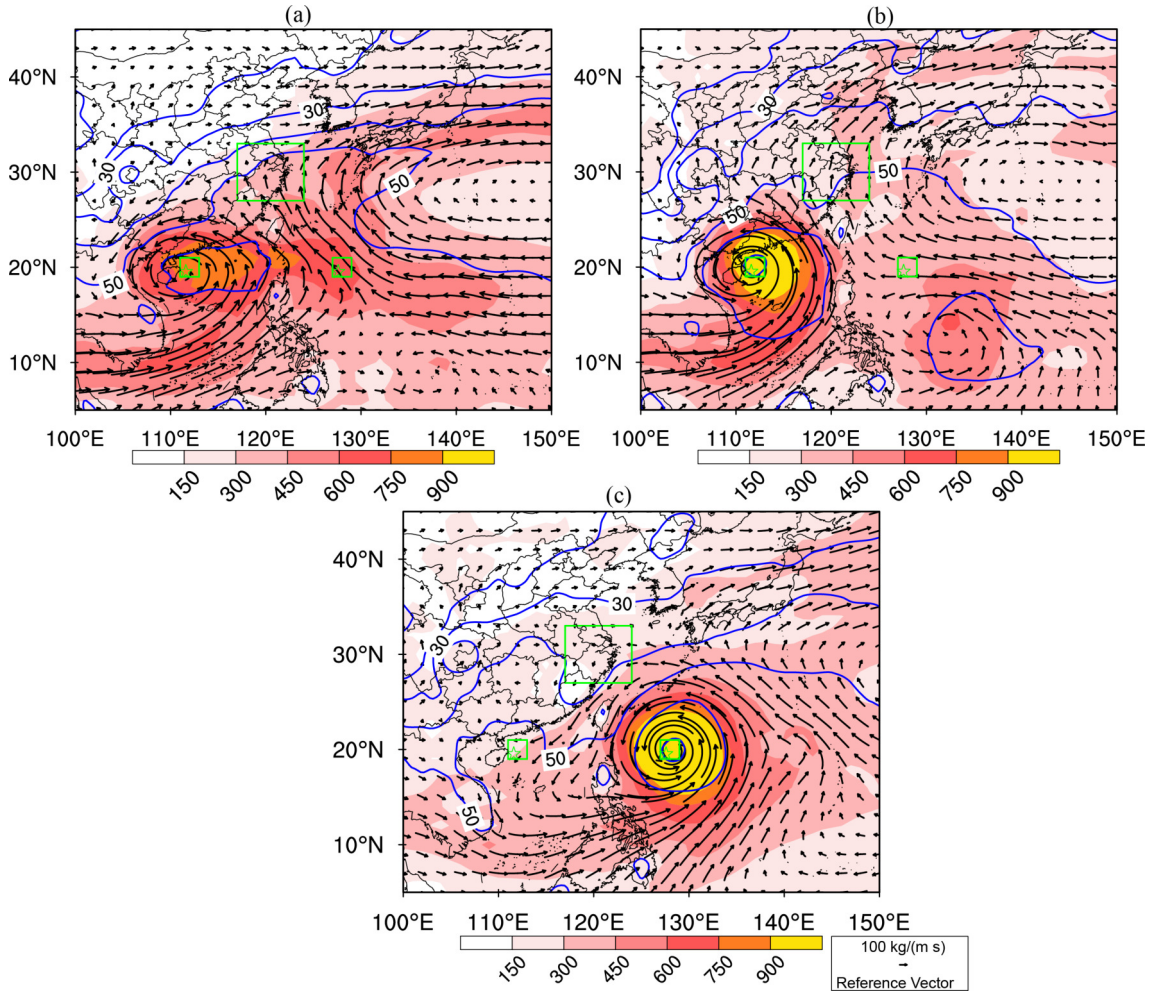

Fig. 9. Composite total-column precipitable water (contours, mm), column-integrated water vapor flux (vectors, kg m^{-1} s^{-1}), and column-integrated water vapor flux (shaded, kg m^{-1} s^{-1}) for (a) predecessor rain event (PRE) cases, (b) northwestward moving TCs passing through the domain of 19°–21°N and 111°–113°E but not associated with heavy rainfall in the YRD region (NPRE cases), and (c) northward moving TCs passing through the domain of 19°–21°N and 127°–129°E but not associated with heavy rainfall in the YRD region (NPRE_NE cases). The rectangles denote the same regions as in Fig. 4.

significantly different in the SCS and PRE regions (Fig. 9e). In contrast, northeasterly winds prevail for NPRE_NE cases; the corresponding column-integrated water vapor flux was 200 kg m^{-1} s^{-1} and precipitable water was approximately 40 mm (Fig. 9c). A student's *t*-test showed that the TPW between NPRE_NE and NPRE cases were significantly different in the SCS and PRE regions (Fig. 9f).

To analyze the differences in low-level water vapor transport between the PRE and NPRE cases, an analysis for low-level synoptic environments was further conducted in Fig. 10. Equivalent potential temperature isotherms were densely packed from the TC to the YRD region; correspondingly, the low-level baroclinic zone stretched northeastward from the TC to the YRD region for PRE cases (Fig. 10a). With its orientation shifted southward and eastward, the baroclinic zone was still present for NPRE_NE cases stretching northeastward from Taiwan to the East China Sea (Fig. 10b). For NPRE cases, the equivalent potential temperature isotherms were sparsely distributed in the YRD region (Fig. 10c). The difference of equivalent potential temperature between PRE and NPRE cases further showed that northeasterly flow from the north was blowing toward the YRD region, and 925 hPa southeasterly flow from the Ocean was also blowing toward the PRE region. Compared to the NPRE cases, 925 hPa northeasterly winds and southeasterly winds were prevalent for the PRE cases in the YRD region (Fig. 10d); whereas compared to the NPRE_NE cases, southerly winds were conspicuous for the PRE cases in the YRD region (Fig. 10e). Comparison of NPRE and NPRE_NE showed that the existence of a SCS TC or a WNPO TC was not sufficient to produce a PRE in the YRD region (Fig. 10f). This suggests that both 925 hPa northeasterly flow from the north and southeasterly flow from the Ocean are significant for the occurrence of PREs in the YRD region. Frontogenesis occurring in the YRD region and south of the East China Sea was in response to densely

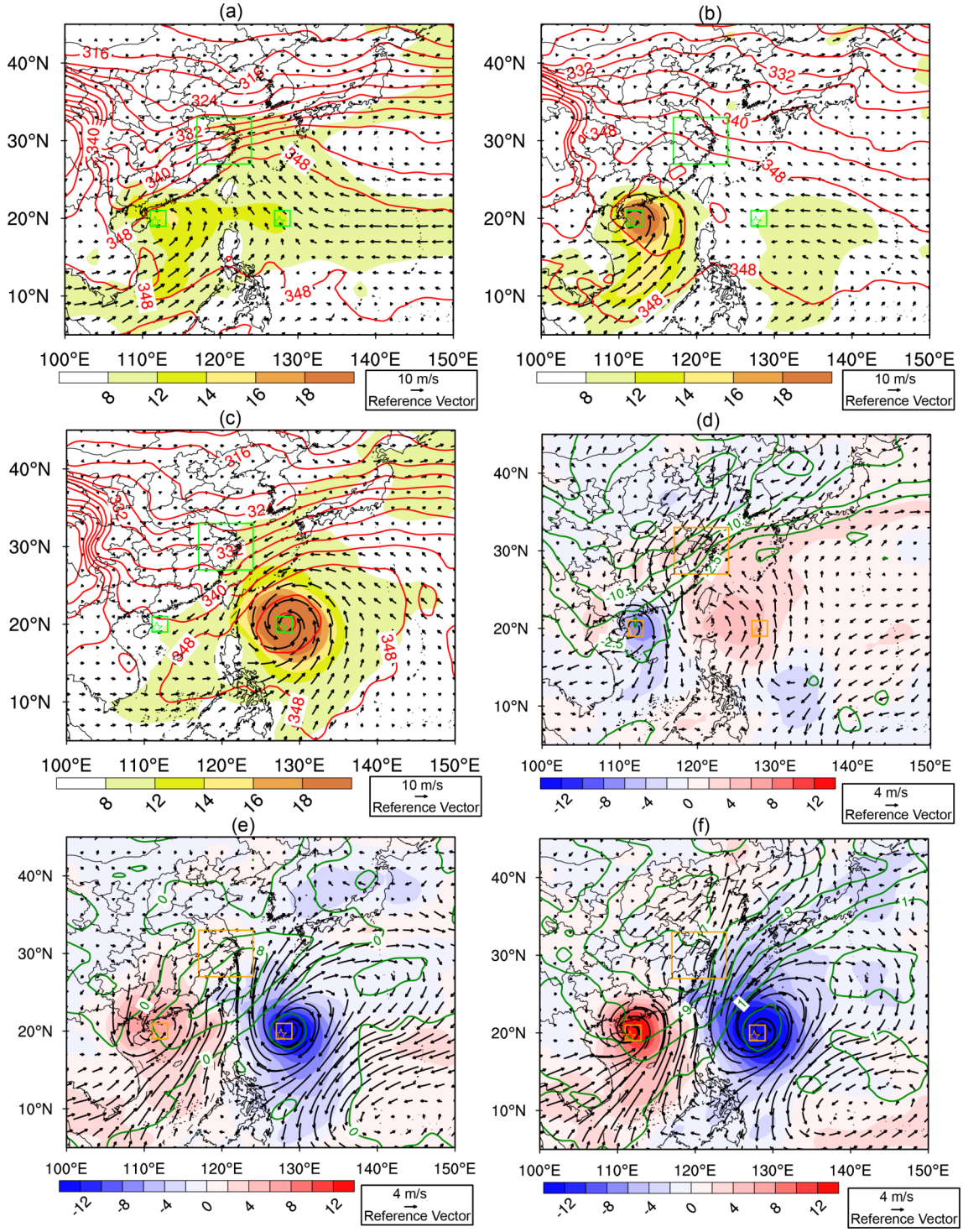

Fig. 10. Composite 925 hPa wind (vectors), wind speed (shaded), and equivalent potential temperature (contours, K) for all (a) predecessor rain event (PRE) cases, (b) northwestward moving TCs passing through the domain of 19°–21°N and 111°–113°E but not associated with heavy rainfall in the YRD region (NPRE cases), and (c) northward moving TCs passing through the domain of 19°–21°N and 127°–129°E but not associated with heavy rainfall in the YRD region (NPRE_NE cases), and their differences between (d) PRE and NPRE (PRE − NPRE), (e) PRE and NPRE_NE (PRE − NPRE_NE), (f) NPRE_NE and NPRE(NPRE − NPRE_NE). The units are m s^{-1} for wind vectors and wind speeds. The rectangles denote the same regions as in Fig. 4.

packed equivalent potential temperature isotherms for the PRE cases (Fig. 11a); however, frontogenesis did not occur in the YRD region for NPRE and NPRE_NE cases (Fig. 11b, and Fig. 11c). A convergence of column-integrated water vapor flux was observed in the region where deep tropical moisture transported by southeasterly flows intersects a low-

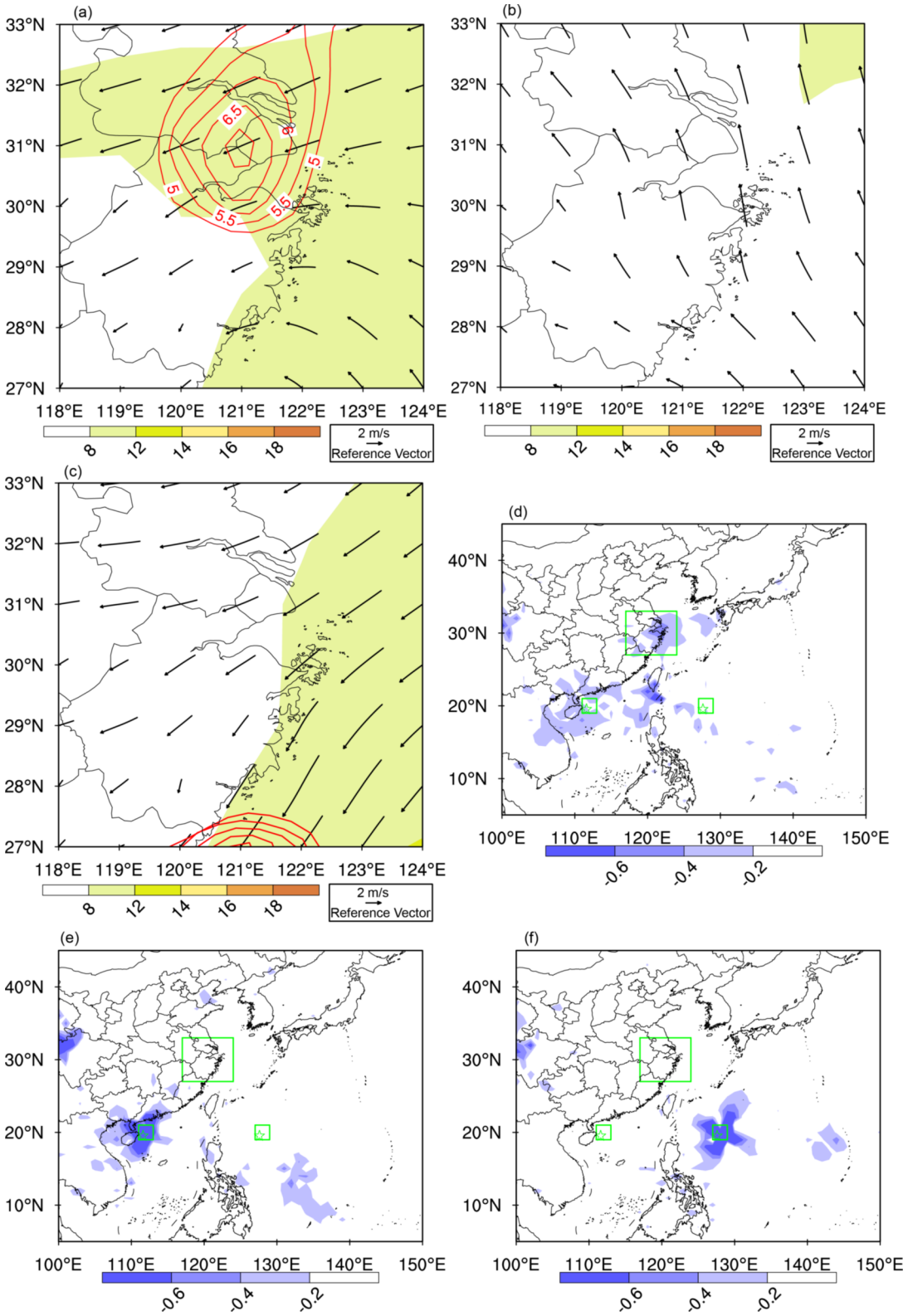

Fig. 11. The composite 925 hPa wind (vectors), wind speed (shaded, m s^{-1}), and frontogenesis (red contours, 10^{-6} K m^{-1} s^{-1}) for all (a) predecessor rain event (PRE) cases, (b) north-westward moving TCs passing through the domain of 19°–21°N and 111°–113°E but not associated with heavy rainfall in the YRD region (NPRE cases), and (c) northward moving TCs passing through the domain of 19°–21°N and 127°–129°E but not associated with heavy rainfall in the YRD region (NPRE_NE cases), and divergence of column-integrated water vapor flux (shaded, g m^{-2} s^{-1}) for (d) PRE, (e) NPRE, and (f) NPRE_NE cases. The rectangles denote the same regions as in Fig. 4.

level baroclinic zone that stretched northeastward from the TC vicinity to the YRD region (Fig. 11d), with a divergence of < -0.6 g m^{-2} s^{-1}. Conversely, neither the low-level southeasterly feed of deep tropical moisture (Fig. 11e) nor the low-level baroclinic zone (Fig. 11f) alone was sufficient to produce water vapor flux divergence. Galarneau et al. (2010) and Yuan et al. (2018) showed that the upper-level jet played an important role in generating PREs associated with TCs. To examine the mechanisms driving heavy rainfall of PREs, the upper-level synoptic environment was further analyzed.

5. Influence of 200-hPa westerly jet

Figure 12 shows the composite of 200-hPa geopotential height and jet structure. At 200 hPa, an upper-level westerly jet located over East Asia between 30°N and 40°N, stretching from China's coastal areas to the Sea of Okhotsk, was present for PRE cases (Fig. 12a). A two-sided student's *t*-test for the PREs compared to the weighted monthly long-term (2010–19) climatology suggests that the 200-hPa geopotential height and 200-hPa winds of the PREs in the YRD region were statistically significant at the 95% level (Fig. 12d). The westerly jet was also present for NPRE and NPRE_NE cases and was respectively orientated eastward and northward between 35°N and 45°N, but they were much weaker than that in PRE cases (Figs. 12b, 12c). The composite PRE in the YRD region was initiated in the equatorward jet entrance region of a 200-hPa jet with wind speeds exceeding 45 m s^{-1}. This configuration is conducive to upward motion because the entrance region of a straight upper-level jet streak exhibits upward motion according to quasi-geostrophic theory. This vertical motion is beneficial for moistening and destabilization (Uccellini and Johnson, 1979; Bosart and Lackmann, 1995; Galarneau et al., 2010). Conversely, favorable environments for ascent in the YRD region were absent for NPRE and NPRE_NE cases owing to the northeastward displacement of the 200-hPa jet. A Student's *t*-test for PRE and NPRE cases showed that significant differences in 200-hPa geopotential heights appeared from south of the SCS region, PRE region, and mid-latitudes (Fig. 12e). The 200-hPa zonal winds, in particular, exhibited significant differences in middle latitudes between 30°–40°N. The locations and strengths of the upper-level westerly jet were different between PRE and NPRE cases. A Student's *t*-test for NPRE and NPRE_NE cases showed that significant differences in 200-hPa geopotential heights appeared from south of the SCS region, PRE region, and mid-latitudes (Fig. 12f). The 200-hPa zonal winds especially showed significant differences in middle latitudes between 30°–40°N, and it indicated that the locations and strengths of the upper-level westerly jet were also quite different between NPRE and NPRE_NE cases.

The formation of the stronger 200-hPa westerly jet in PREs in the YRD region can be explained from Figs. 13–15, which show the composite analyses of 250–200 hPa averaged synoptic environments generated using 6-hourly NCEP FNL reanalysis data at the times when PREs occurred (T+0), 24 h prior to PRE occurrence (T–24 h), and 24 h after PREs occurrence (T+24 h). The spatial area with wind speeds of 200-hPa westerly jet exceeding 50 m s^{-1} was conspicuously larger, and it strengthened from 54 to 57 m s^{-1} from T–24 to T+0 (Fig.12a; Figs. 13a, 13c). The maintenance of the 200-hPa westerly jet was favorable to the occurrence of PREs in the YRD region. Specifically, the occurrence of PREs in the YRD region was associated with strongly divergent outflow and upward motion at upper levels forced by intense latent heat release. Previous studies pointed out that the upper-level diabatically driven outflow may interact with a 200-hPa westerly jet, since such outflow from a heavy rainfall-producing weather system can influence upper-level westerly jet by impacting the potential vorticity (PV) gradient along the jet streak (Galarneau et al., 2010; Bosart et al., 2012; Moore et al., 2013; Yuan et al., 2018). The formulation of PV applied in this study follows that given by Bluestein (1992).

Following the methods used by Galarneau et al. (2010), Bosart et al. (2012), Moore et al. (2013), and Yuan et al. (2018), composite analyses of 200–250 hPa layer-averaged divergent winds and negative PV advection by the divergent winds were computed in Fig. 15 to explain the formation of the enhanced 200-hPa westerly jet (Figs. 12a, 13b, and 13c). Specifically, the winds were decomposed into divergent and non-divergent components, and the divergent winds for PREs, NPREs, and NPRE_NE cases as shown in Fig. 14.

Strong southeasterly divergent winds from the YRD region were transported to the 200-hPa jet-entrance region for the PRE cases (Fig. 14a), while southwesterly divergent winds from the East China Sea were transported into the 200-hPa jet-entrance region for the NPRE_NE cases (Fig. 14c). This was in response to eastward movement of the upper-level trough to the YRD region and East China Sea region for PREs and NPRE_NE cases, respectively (Figs. 14a, 14c). The absence of an upper-level trough in the East China is coincident with the absence of divergent winds at the 200-hPa jet entrance for the NPRE cases (Fig. 14b). Note that upstream upper-level troughs were present for PRE and NPRE_NE cases but were absent for NPRE cases. Hardly any outflows in the TC vicinity of the South China Sea were transported into the 200-hPa jet region for the NPRE cases. According to the above considerations, the presence of the 200-hPa westerly jet was likely associated with the approach of an upstream upper-level trough, and the TC-related diabatically driven outflow was not dominant. This may differ from the conclusion that the 200-hPa westerly jet closely related to PREs was directly influenced by the approach of the upstream trough and TC-related diabatically driven outflow (Galarneau et al., 2010; Yuan et al., 2018). The 200-hPa westerly jet occurred in conjunction with the approach of the upstream mid-latitude trough, indicating that the dynamical process of wave-flow interaction in mid-high latitudes may be important for the westerly jet anomalies

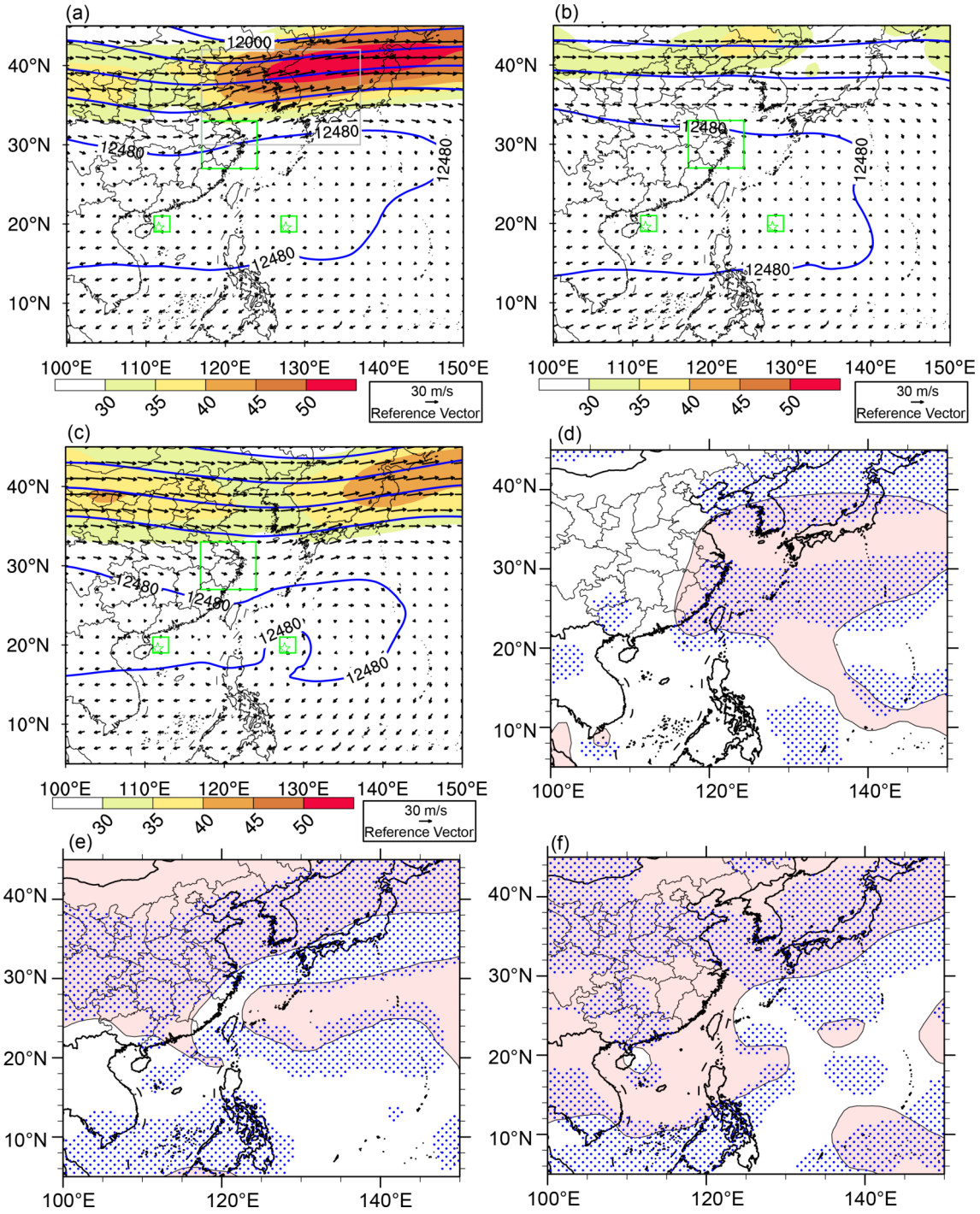

Fig. 12. Composite analyses at 200 hPa of geopotential height (solid lines, gpm), winds (vectors), and wind speed (shaded) for (a) predecessor rain event (PRE) cases, (b) northwestward moving TCs passing through the domain of 19°–21°N and 111°–113°E but not associated with heavy rainfall in the YRD region (NPRE cases), and (c) northward moving TCs passing through the domain of 19°–21°N and 127°–129°E but not associated with heavy rainfall in the YRD region (NPRE_NE cases); (d) the significant *t*-test of the difference between PRE and the weighted monthly long-term (2010–19) climatology for geopotential heights and zonal wind component, where blue dots denote the difference of 200 hPa zonal wind component and red shading depicts 200 hPa geopotential height differences; (e) similarly for PRE and NPRE cases, and (f) for NPRE_NE and NPRE cases. Composite tropical cyclone locations are indicated by pentagrams. Shading indicates wind speeds at 200 hPa (m s^{-1}). The rectangular box denotes the position of the PREs in the YRD region. The rectangles denote the same regions as in Fig. 4.

(Gao et al., 1990; Yang et al., 2015).

To further explain the intensification of the 200-hPa westerly jet from *T*–24 to *T*+0 h, the negative PV advection by the divergent winds was computed (Fig. 15) at *T*+0, *T*–24,

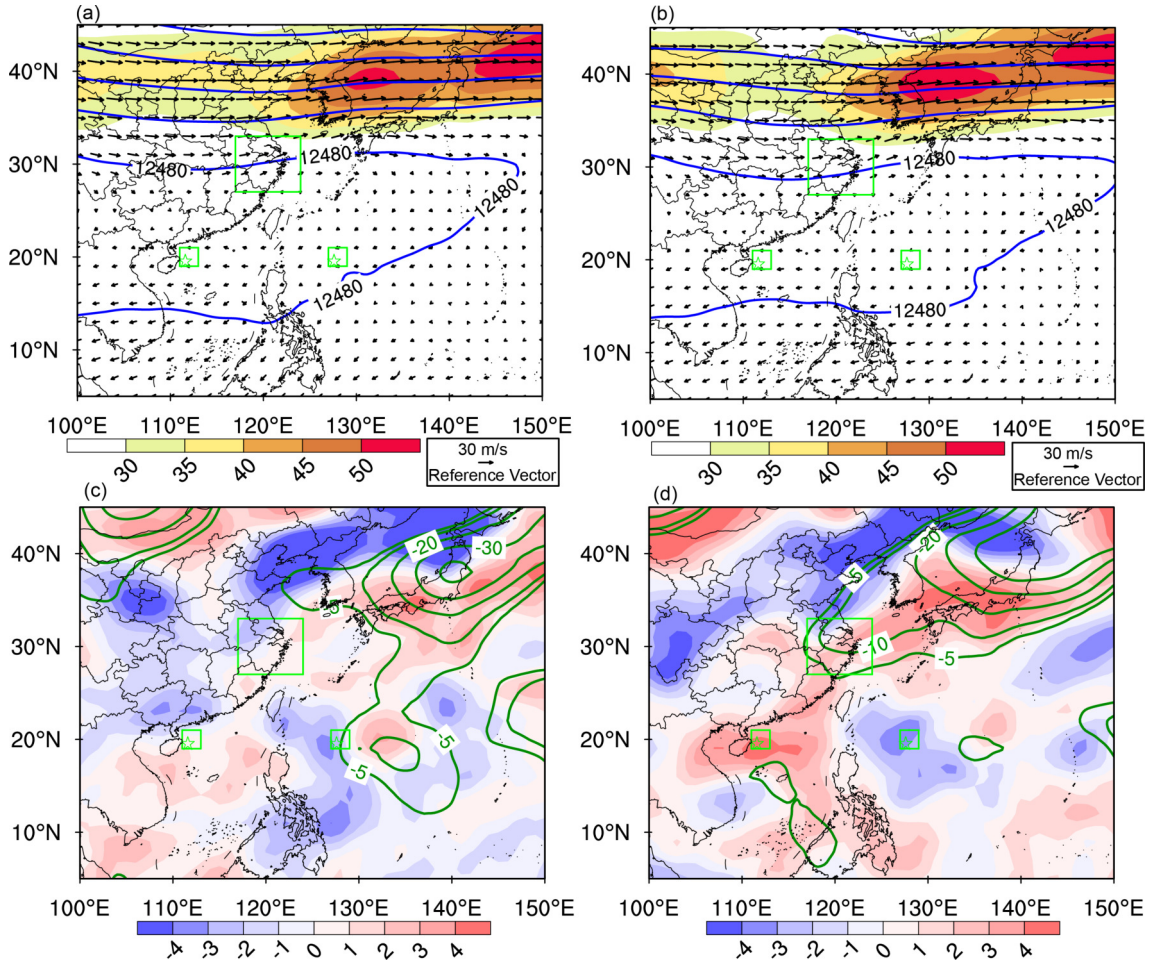

Fig. 13. Composite 200 hPa geopotential height (solid lines, gpm) , winds (vectors), and wind speed (shaded, m s^{-1}) for predecessor rain event (PRE) cases at (a) *T*–24, and (b) *T*+24; The differences of 200 hPa geopotential height are shown as green contours every 10.0 gpm starting at –5.0 gpm and wind speed as shading for (c) *T*–24 vs. *T*+0, and (d) *T*+24 vs. *T*+0. Composite tropical cyclone locations are indicated by pentagrams. Shading indicates wind speeds at 200 hPa (m s^{-1}). The rectangular box denotes the position of the PREs in the YRD region. The rectangles denote the same regions as in Fig. 4.

and *T*+24 h. During the PREs occurring at *T*+0 h, the 200-hPa westerly jet was to the northeast of the YRD region, and strong ascent associated with low PV existed in the equatorward entrance region of the 200-hPa westerly jet (Figs. 15a–b). Divergent winds were directed outward from the YRD region of ascent where PREs occurred in the jet entrance region with larger values of PV, corresponding to the negative PV advection by divergent winds therein (Figs. 15a–b). From *T*–24 to *T*+0 h, accompanied by the initiation of PREs in the YRD region, low-PV in the YRD region expanded to the high-PV 200-hPa jet streak region, corresponding to the meridionally strengthened PV gradient (Figs. 15a–b). Concurrently, the enhanced negative PV advection in association with strengthened divergent winds expanded from the YRD region, which corresponded to the intensification of the 200-hPa westerly jet (Figs. 15a–b). Therefore, the negative PV advection was linked to the diabatic outflow of the PREs by divergent winds, it was mainly located in the equatorward entrance region of 200-hPa westerly jet, and thus, it likely contributed to the meridionally increased PV gradient as a result of the enhanced 200-hPa westerly jet.

From *T*+0 to *T*+24 h, the diabatically driven outflow originating from the YRD region to the 200-hPa westerly jet streak decreased (Figs. 15a, 15c), and the divergent winds and PV advection also decreased, accompanying the eastward movement of the 200 hPa-westerly jet from west of the Korean Peninsula to its east (Figs. 15a, 15c). Concurrently, the associated ascent decreased in the YRD region, accompanied by the eastward movement of the 200-hPa westerly jet.

Most importantly, the upper-level westerly jet existed before moving to the north of the YRD region, and it strengthened as it propagated eastward in conjunction with the approach of the mid-latitude trough. The pre-existence of an upper-level westerly jet over to the north of the YRD region may be favorable for the occurrence of PREs in the YRD region. Simultaneously, the occurrence of heavy rainfall in the YRD region may be conducive to the maintenance of

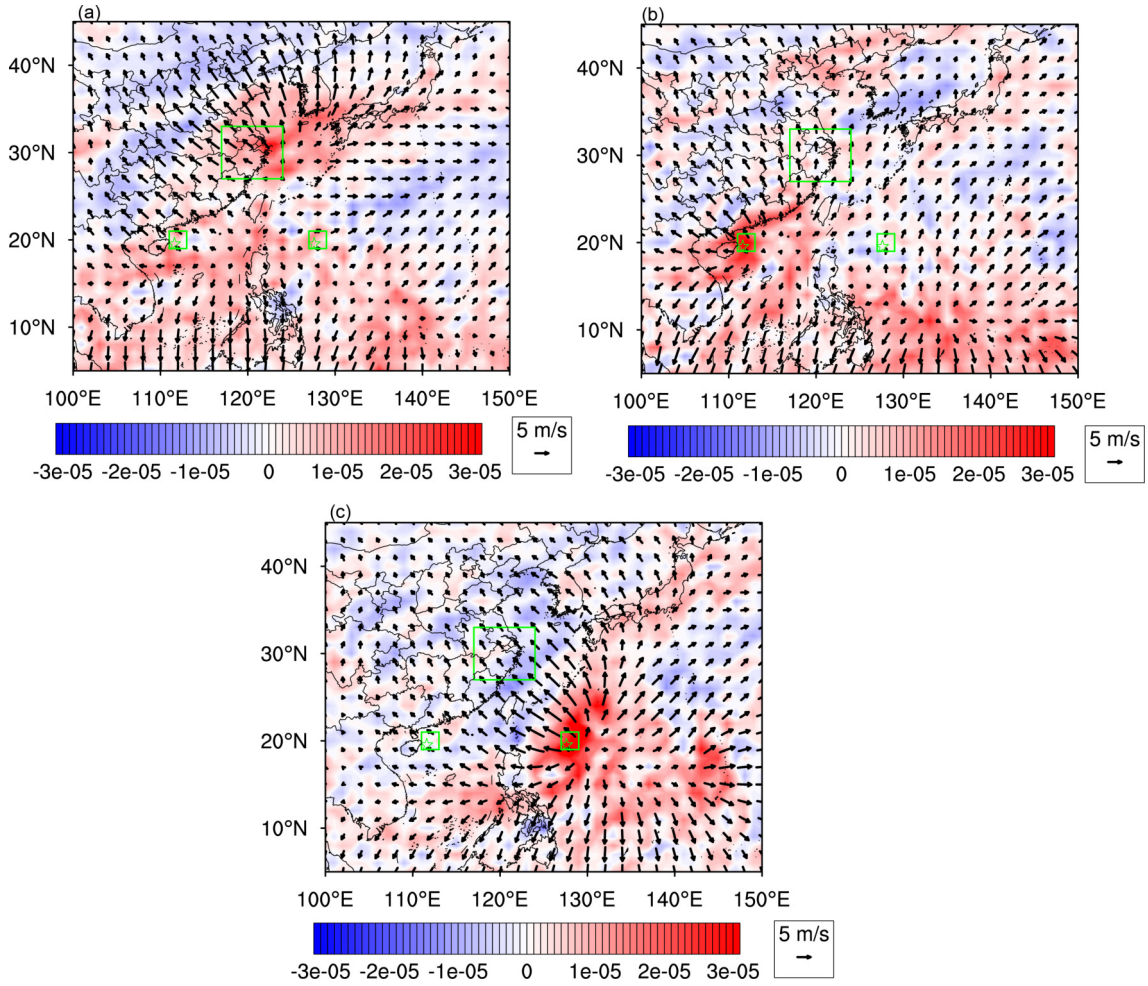

Fig. 14. Composite 200–250 hPa layer-averaged divergence (shaded, s^{-1}) and divergent wind components (vectors) for (a) predecessor rain event (PRE) cases, (b) northwestward moving TCs passing through the domain of 19°–21°N and 111°–113°E but not associated with heavy rainfall in the YRD region (NPRE cases), and (c) northward moving TCs passing through the domain of 19°–21°N and 127°–129°E but not associated with heavy rainfall in the YRD region (NPRE_NE cases). Composite tropical cyclone (TC) locations are indicated by pentagrams, and the rectangular box denotes the position of the PREs in the YRD region. The rectangles denote the same regions as in Fig. 4.

the upper-level westerly jet northward of the YRD region. The upper-level westerly jet weakened and moved eastward with the ending of PREs.

6. Conclusions

In this study, the synoptic-scale environments of PREs occurring in the Yangtze River Delta during 2010–19 in association with SCS-WNPO TCs were examined through composite analyses. Statistics of the PREs over the YRD region showed that PREs in the YRD region were more likely to occur in June and September when cold air from the North and warm air from the Ocean were comparable in strength in the YRD region. The PREs accompanied TCs with different intensities, but they occurred more commonly with TCs that reach the intensity of a Typhoon. This indicates that the TCs intensity may influence the occurrence of PREs by providing abundant warm tropical moisture to the PRE regions. The PREs occurred frequently in the YRD region when SCS-WNPO TCs tracked northwestward to the South China Sea. SCS-WNPO TCs could produce a median value of 201 mm total PRE precipitation in the YRD region for the PREs. The distances between the parent TCs and PREs varied widely, with a wide distance ranging from 889 to 1730 km and a median distance of approximately 1388 km. These statistical results may provide a climatology guideline for weather forecasters to predict PREs in the YRD region, where models and forecasters often failed to predict PREs correctly. The statistical results can also provide a reference for the forecasters about how long before the TC the PRE will occur, and how long the PRE will last once it is initiated in the coastal areas of China.

The key factors beneficial to the occurrence of PREs in the YRD region include a specific configuration of a westward stretching of the Western North Pacific subtropical high, 500-hPa mid-latitude westerly trough, 200-hPa westerly

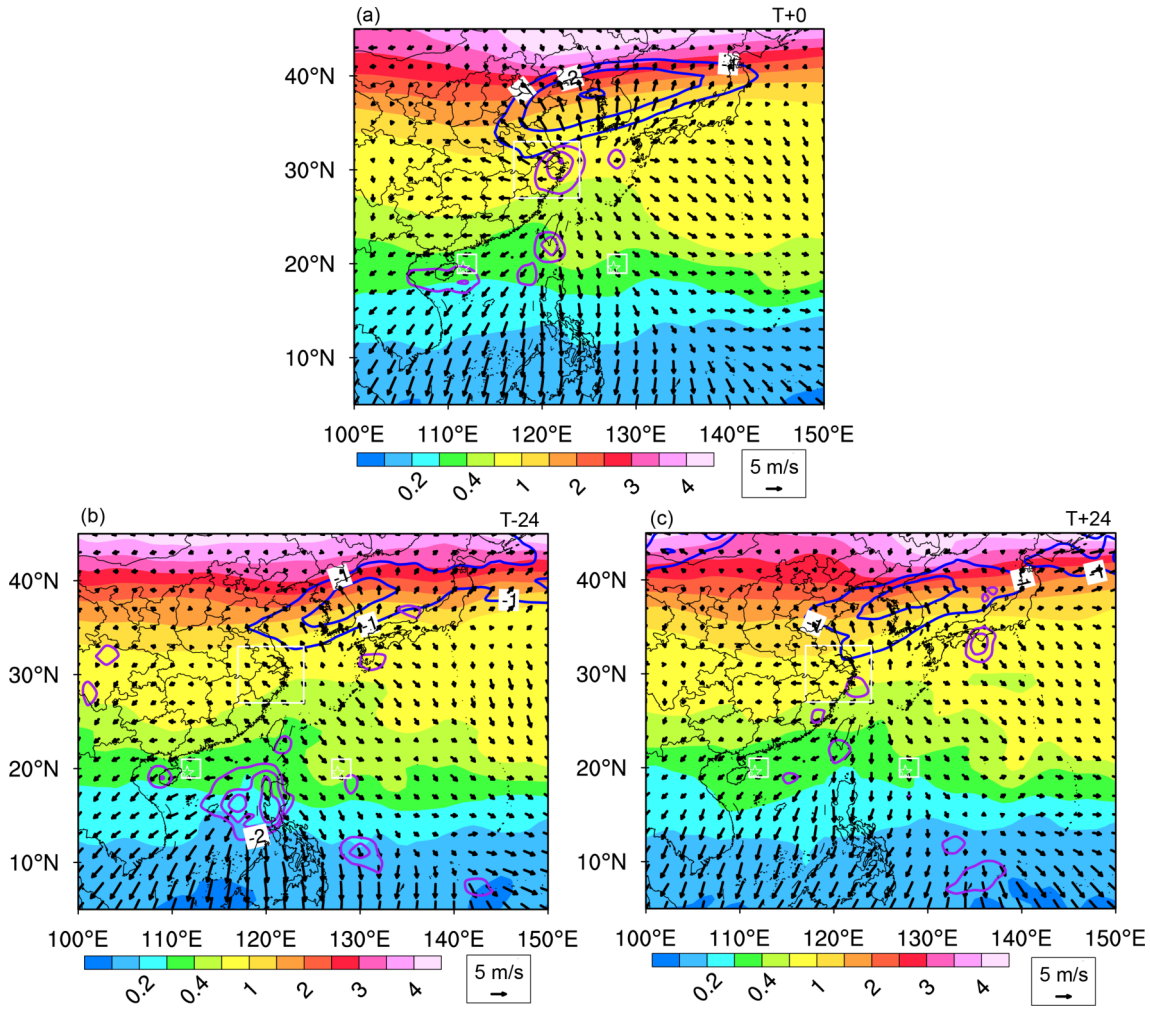

Fig. 15. Composites for PREs showing 250–200 hPa layer-averaged divergent winds (vectors, m s^{-1}), and 700–500 hPa layer-averaged ascent (purple contours starting at -2×10^{-1} Pa s^{-1} every -1×10^{-1} Pa s^{-1}), PV in the 250–200 hPa layer (shaded every 1PVU, where 1PVU=10^6 K m^2 kg^{-1} s^{-1}), and PV advection by divergent wind in the 250–200 hPa layer (negative values contoured in blue every –0.1 PVU d^{-1} starting at –0.1PVU d^{-1}) at (a) *T*+0, (b) *T*–24, and (c) *T*+24 h. Composite tropical cyclone (TC) locations are indicated by pentagrams, and the rectangular box denotes the position of the PREs in the YRD region.

Table 1. All documented PREs associated with SCS-WNPO TCs during 2010–19. Listed are initiation time and date, TC number, TC name, and geographical area when PRE occurred in the YRD region.

TC (year)	TC number	initiation time (UTC) and date	geographical area	end time (UTC) and date
Nalgae (2011)	1119	0600 UTC 29 Sep	WNPO	0600 UTC 30 Sep
Guchol (2012)	1204	1800 UTC 16 Jun	WNPO	0600 UTC 18 Jun
Talim (2012)	1205	1800 UTC 16 Jun	SCS	0600 UTC 18 Jun
Bebinca (2013)	1305	0600 UTC 23 Jun	SCS	0000 UTC 24 Jun
Danas (2013)	1324	1800 UTC 06 Oct	WNPO	0000 UTC 08 Oct
Fung-Wong (2014)	1416	0000 UTC 20 Sep	SCS	0000 UTC 21 Sep
Linfa (2015)	1510	0000 UTC 06 Jul	SCS	1800 UTC 06 Jul
Meranti (2016)	1614	0600 UTC 13 Sep	SCS	0000 UTC 14 Sep
Khanun (2017)	1720	1800 UTC 14 Oct	SCS	0000 UTC 16 Oct
Mangkhut (2018)	1822	0000 UTC 16 Sep	SCS	0600 UTC 17 Sep
Podul (2019)	1912	1200 UTC 28 Aug	SCS	0600 UTC 29 Aug
Lingling (2019)	1913	0000 UTC 02 Sep	SCS	1800 UTC 02 Sep

jet, and the intensification of low level southwesterly or southeasterly flow. Specifically, when PREs occurred in the YRD region: the Western North Pacific subtropical high was dominant in the WNPO with the westernmost point extending eastward to 120°E; a mid-latitude long-wave trough moved eastward, and the YRD region was located in front of the trough; and the YRD PREs formed beneath an equatorward upper-level westerly jet entrance region on the western flank of a 925-hPa equivalent potential temperature ridge. The 925-hPa southeasterly tropical flow was nearly perpendicular to the equivalent potential temperature isotherms, which can be regarded as a baroclinic zone. This flow was located between the westerly trough and the Western North Pacific subtropical high, and it contributed to the PREs occurrence by transporting deep tropical moisture poleward and enhancing low-level convergence, frontogenetical forcing, and ascending motions occur over the YRD region. Additionally, the upper-level westerly jet situated north of the YRD region probably played a prominent role in the formation of PREs, because of strong ascending motion beneath the equatorward entrance region of the upper-level westerly jet. The upper-level westerly jet intensified in association with the diabatically driven outflow related to the PREs, the enhanced pressure gradient due to the diabatic outflow, and the maintenance of the upstream upper-level trough.

Galarneau et al. (2010) summarized that PREs in the United States to the east of the Rockies generally form in the equatorward entrance region of a 200-hPa jet, and they occur at the intersection of the 925-hPa equivalent potential temperature ridge and tropical moisture flow where frontogenesis and ascent occur. Moore et al. (2013) further summarized that PREs generally occur when deep tropical moisture is transported to the baroclinic zone beneath the equatorward jet-entrance region of a 200-hPa jet. Yuan et al. (2018) concluded that Bay of Bengal TC-related PREs over China's low-latitude highlands bear similar key configurations, and their study also emphasized the importance of terrain lifting in the initiation of PREs there. The composite synoptic-scale environment for PREs in the YRD region exhibits some similarities to PREs investigated by Galarneau et al. (2010) and Yuan et al. (2018) in China's low-latitude highlands, which are associated with the Bay of Bengal tropical storms.

The present study showed that the atmosphere features in the vicinity of the PREs in YRD includes an enhanced upper-level jet ahead of the mid-latitude trough, a large amount of moisture transported from the tropical parent TCs, and local frontogenetical forcing. Despite the common characteristics of the configuration of atmosphere features for the PREs in the YRD region with those in Galarneau et al. (2010), Moore et al. (2013), and Yuan et al. (2018), there may be some differences between this study and the above studies in some respects. This study indicated that the preexistence of the upper-level jet to the northeast of the YRD region was favorable to the occurrence of PREs, and in turn, the occurrence of PREs contributed to the intensification of the upper-level westerly jet by diabatically driven divergent outflow. The TC outflows probably played a secondary role or did not directly affect the upper-level jet.

Despite the existence of TCs in the SCS region for the NPREs, the upper-level westerly jet in the mid-high latitudes did not strengthen, and this also indicated that the TC outflow was not dominant in the intensification of the upper-level westerly jet in the mid-high latitudes. Additionally, the intensity of low-level southwesterly flow may not reach 12 m s^{-1} during the PREs occurrences in the YRD region, which may differ from Galarneau et al. (2010) who found the low-level jet can be 20 m s^{-1}.

This study aimed to provide guidelines to predict heavy rainfall associated with SCS-WNPO TCs over the YRD region. Caution should be exercised that the results were based on statistics and composite analysis, and numerical experiments may be necessary to further quantify the effect of moisture from the vicinity of TCs in producing PREs in the YRD region. Sensitivity tests to remove the TC vortex from the model simulation need to be conducted to further confirm that TCs do not directly contribute significantly to the intensification of the 200-hPa westerly jet. We will analyze more predecessor rainfall events over longer periods to further confirm the above conclusions in the near future.

Acknowledgements. The data used in this study are available at the training center of atmospheric sciences of Zhejiang University Best track data which can be accessed at http://www.jma.go.jp/jma/jma-eng/jma-center/rsmc-hp-pub-eg/besttrack.html. NCEP FNL data with 1°×1° horizontal resolution were obtained from the NCAR UCAR Research Data Archive Computational and Information System Lab (https://rda.ucar.edu/). Hourly rainfall data were downloaded from the China Meteorological Data Service Center (http://data.cma.cn/data/cdcdetail/dataCode/SEVP_CLI_CHN_MERGE_CMP_PRE_HOUR_GRID_0.10.html) in June 2021. This work was supported by the National Natural Science Foundation of China (Grant Nos. 42105004, 41930967, 42192554, and 42105011), the Natural Science Foundation of Zhejiang Province of China (Grant No. LQ20D050001), and the Scientific Research Foundation of Hangzhou Normal University (Grant No. 2020QDL015).

REFERENCES

Bao, X. W., and Coauthors, 2015: Diagnostics for an extreme rain event near Shanghai during the landfall of Typhoon Fitow (2013). *Mon. Wea. Rev.*, **143**(9), 3377–3405, https://doi.org/10.1175/MWR-D-14-00241.1.

Bluestein, H. B., 1992: *Synoptic-Dynamic Meteorology in Midlatitudes: Volume 1, Principles of Kinematics and Dynamics*. Oxford University Press, 448 pp.

Bosart, L. F., and F. H. Carr, 1978: A case study of excessive rainfall centered around Wellsville, New York, 20–21 June 1972. *Mon. Wea. Rev.*, **106**(3), 348–362, https://doi.org/10.1175/1520-0493(1978)106<0348:ACSOER>2.0.CO;2.

Bosart, L. F., and G. M. Lackmann, 1995: Postlandfall tropical cyclone reintensification in a weakly baroclinic environment: A case study of Hurricane David (September 1979). *Mon.*

Wea. Rev., **123**(11), 3268–3291, https://doi.org/10.1175/1520-0493(1995)123<3268:PTCRIA>2.0.CO;2.

Bosart, L. F., J. M. Cordeira, T. J. Galarneau, B. J. Moore, H. M. Archambault, 2012: An analysis of multiple predecessor rain events ahead of Tropical Cyclones Ike and Lowell: 10–15 September 2008. *Mon Wea Rev*, **140**(4), 1081–1107, https://doi.org/10.1175/MWR-D-11-00163.1.

Byun, K. Y., and T. Y. Lee, 2012: Remote effects of tropical cyclones on heavy rainfall over the Korean peninsula-statistical and composite analysis. *Tellus A: Dynamic Meteorology and Oceanography*, **64**(1), 14983, https://doi.org/10.3402/tellusa.v64i0.14983.

Chang, C. P., L. Yi, and G. T. J. Chen, 2000: A numerical simulation of vortex development during the 1992 East Asian summer monsoon onset using the Navy's regional model. *Mon. Wea. Rev.*, **128**(6), 1604–1631, https://doi.org/10.1175/1520-0493(2000)128<1604:ANSOVD>2.0.CO;2.

Chen, L. S., 2007: Study and forecast on Landfall tropical cyclone heavy rainfall. *Proc. 14th Proseminar on Tropical Cyclone*, Shanghai, 3–7. Available from https://d.wanfangdata.com.cn/conference/7187768 on June, 2021. (in Chinese)

Chen, S. Q., Y. Li, Y. M. Fan, Z. Y. Xu, and F. Li, 2021: Analysis of long-distance heavy rainfall caused by Typhoon Mangosteen (2018). *Chinese Journal of Atmospheric Sciences*, **45**(3), 573–587, https://doi.org/10.3878/j.issn.1006-9895.2009.20126. (in Chinese with English abstract)

Cheng, J. B., Y. H. Zhao, R. Zhi, and G. L. Feng, 2022: Analysis of the July 2021 extreme precipitation in Henan using the novel moisture budget equation. *Theor. Appl. Climatol.*, **149**, 15–24, https://doi.org/10.1007/s00704-022-04022-7.

Chien, F. C., 2014: A numerical study on the slow translation speed of Typhoon Morakot (2009). *SOLA*, **10**, 190–193, https://doi.org/10.2151/sola.2014-040.

CMA: China Meteorological Administration (CMA), 2011: Continuing from 2008, Research Data Archive at China Meteorological Data Service center for sharing meteorological data resources. Available from http://data.cma.cn/site/showSubject/id/101.html on June, 2021. (in Chinese)

Cong, C. H., L. S. Chen, X. T. Lei, and Y. Li, 2012: A study on the mechanism of the tropical cyclone remote precipitation. *Acta Meteorologica Sinica*, **70**(4), 717–727, https://doi.org/10.11676/qxxb2012.058. (in Chinese with English abstract)

Cote, M. R., 2007: Predecessor rain events in advance of tropical cyclones. M.S. thesis, Department of Atmospheric and Environmental Sciences, University at Albany, State University of New York.

Cui, C. G., X. Q. Dong, B. Wang, B. K. Xi, Y. Deng, and Y. H. Ding, 2021: Integrative monsoon frontal rainfall experiment (IMFRE-I): A mid-term review. *Adv. Atmos. Sci.*, **38**(3), 357–374, https://doi.org/10.1007/s00376-020-0209-1.

Ding, Z. Y., X. H. Zhao, X. Rui, and S. Gao, 2017: Statistical analysis of summer tropical cyclone remote precipitation events in East Asia from 2000 to 2009 and numerical simulation. *Journal of Tropical Meteorology*, **23**(1), 37–46, https://doi.org/10.16555/j.1006-8775.2017.01.004.

Draxler, R. R., and G. D. Hess, 1998: An overview of the Hysplit_4 modelling system for trajectories, dispersion, and deposition. *Australian Meteorological Magazine*, **47**, 295–308.

Duan, J. J., Y. Z. Qian, J. J. Jiang, Y. Wang, and Z. L. Wu, 2020: Causes of rainstorm enhancement in northeastern Zhejiang related with Typhoon Khanun landing in Guangdong Province. *Journal of Arid Meteorology*, **38**(5), 737–746, https://doi.org/10.11755/j.issn.1006-7639(2020)-05-0737. (in Chinese with English abstract)

Frank, W. M., 1977: The structure and energetics of the tropical cyclone. I: Storm structure. *Mon. Wea. Rev.*, **105**, 1119–1135, https://doi.org/10.1175/1520-0493(1977)105<1119:TSAEOT>2.0.CO;2.

Galarneau, T. J., L. F. Bosart, and R. S. Schumacher, 2010: Predecessor rain events ahead of tropical cyclones. *Mon. Wea. Rev.*, **138**(8), 3272–3297, https://doi.org/10.1175/2010MWR3243.1.

Gao, S., S. Tao, and Y. Ding, 1990: The generalized E-P flux of wave-mean flow interactions. *Science in China (Chemistry)*, **33**, 704–715 (in Chinese). https://www.cnki.com.cn/Article/CJFDTotal-JBXG199006008.htm

Gao, S. Z., Z. Y. Meng, F. Q. Zhang, and L. F. Bosart, 2009: Observational analysis of heavy rainfall mechanisms associated with severe Tropical Storm Bilis (2006) after its landfall. *Mon. Wea. Rev.*, **137**(6), 1881–1897, https://doi.org/10.1175/2008MWR2669.1.

Geng, B., H. Yamada, K. K. Reddy, H. Uyeda, and Y. Fujiyoshi, 2004: An observational study of the development of a rainband on a Meiyu front causing heavy rainfall in the downstream region of the Yangtze River. *J. Meteor. Soc. Japan*, **82**(4), 1095–1115, https://doi.org/10.2151/jmsj.2004.1095.

Hanley, D., J. Molinari, and D. Keyser, 2001: A composite study of the interactions between tropical cyclones and upper-tropospheric troughs. *Mon. Wea. Rev.*, **129**(10), 2570–2584, https://doi.org/10.1175/1520-0493(2001)129<2570:ACSOTI>2.0.CO;2.

He, B., M. Y. Lou, H. J. Li, X. H. Fan, C. L. Lu, and S. X. Pan, 2020: Research on uncertainty of ensemble forecasts of the far distance torrential rainfall by Typhoon Goni (2015). *Meteorological Monthly*, **46**(1), 15–28, https://doi.org/10.7519/j.issn.1000-0526.2020.01.002. (in Chinese with English abstract)

Herrera, R. G., D. G. Puyol, E. H. MartÍn, L. G. Presa, and P. R. Rodríguez, 2001: Influence of the North Atlantic oscillation on the Canary Islands precipitation. *J. Climate*, **14**(19), 3889–3903, https://doi.org/10.1175/1520-0442(2001)014<3889:IOTNAO>2.0.CO;2.

Hoskins, B. J., M. E. McIntyre, and A. W. Robertson, 1985: On the use and significance of isentropic potential vorticity maps. *Quart. J. Roy. Meteor. Soc.*, **111**, 877–946, https://doi.org/10.1002/qj.49711147002.

Huang, C. Y., C. S. Wong, and T. C. Yeh, 2011: Extreme rainfall mechanisms exhibited by Typhoon Morakot (2009). *Terrestrial, Atmospheric and Oceanic Sciences*, **22**(6), 613–632, https://doi.org/10.3319/tao.2011.07.01.01(tm.

Huang, H. L., M. J. Yang, and C. H. Sui, 2014: Water budget and precipitation efficiency of Typhoon Morakot (2009). *J. Atmos. Sci.*, **71**(1), 112–129, https://doi.org/10.1175/JAS-D-13-053.1.

Huang, S. C., Y. L. Xie, Y. H. Yan, and P. B. Yu, 2021: Study of high water level during Typhoon In-Fa in the sea area of Zhoushan island. *Hydro-Science and Engineering*(6), 1–8, https://doi.org/10.12170/20210915002. (in Chinese with English abstract)

JMA: Japan Meteorological Agency, 2014: RSMC (Regional Specialized Meteorological Center) Tokyo-Typhoon Center (2014), issued tropical cyclone information in Asia and the Western North Pacific region, operated by the Japan Meteoro-

logical Agency within the framework of the World Weather Watch (WWW) Programme of the World Meteorological Organization (WMO). Available from https://www.jma.go.jp/jma/jma-eng/jma-center/rsmc-hp-pub-eg/trackarchives.html.

Joyce, R. J., J. E. Janowiak, P. A. Arkin, and P. P. Xie, 2004: CMORPH: A method that produces global precipitation estimates from passive microwave and infrared data at high spatial and temporal resolution. *Journal of Hydrometeorology*, **5**(3), 487–503,

Knippertz, P., 2004: A simple identification scheme for upper-level troughs and its application to winter precipitation variability in northwest Africa. *J. Climate*, **17**(6), 1411–1418, https://doi.org/10.1175/1520-0442(2004)017<1411:ASISFU>2.0.CO;2.

Kueh, M. T., C. Y. Huang, S. Y. Chen, S. H. Chen, and C. J. Wang, 2009: Impact of GPS radio occultation refractivity soundings on a simulation of Typhoon Bilis (2006) upon landfall. *Terrestrial, Atmospheric and Oceanic Sciences*, **20**(1), 115–131, https://doi.org/10.3319/TAO.2008.01.21.03(F3C.

Lee, D. K., and S. J. Choi, 2010: Observation and numerical prediction of torrential rainfall over Korea caused by Typhoon Rusa (2002). *J. Geophys. Res.: Atmos.*, **115**(D12), D12105, https://doi.org/10.1029/2009JD012581.

Liu, J., J. Xia, D. She, L. Li, and L. Zou, 2019: Evaluation of Six Satellite-based Precipitation Products and Their Ability for Capturing Characteristics of Extreme Precipitation Events over a Climate Transition Area in China. *Remote Sensing*, **11**(12), 1477, https://doi.org/10.3390/rs11121477.

Liu, B. Q., G. X. Chen, W. X. Zeng, L. Q. Bai, and H. L. Qin, 2022a: Diurnal variations of southerly monsoon surge and their impacts on East Asian summer rainfall. *J. Climate*, **35**(1), 159–177, https://doi.org/10.1175/JCLI-D-21-0372.1.

Liu, Q., H. Q. Xu, and J. Wang, 2022b: Assessing tropical cyclone compound flood risk using hydrodynamic modelling: A case study in Haikou City, China. *Natural Hazards and Earth System Sciences*, **22**(2), 665–675, https://doi.org/10.5194/nhess-22-665-2022.

Lu, X. Q., H. Yu, M. Ying, B. K. Zhao, S. Zhang, L. M. Lin, L. N. Bai, and R. J. Wan, 2021: Western North Pacific tropical cyclone database created by the China Meteorological Administration. *Adv. Atmos. Sci.*, **38**(4), 690–699, https://doi.org/10.1007/s00376-020-0211-7.

Luo, L. J., 2018: Study on the mechanism of a typhoon rainstorm process. M.S. thesis, School of Atmospheric Sciences, Nanjing University of Information Science & Technology. (in Chinese with English abstract)

McBride, J. L., and R. Zehr, 1981: Observational analysis of tropical cyclone formation. Part II: Comparison of non-developing versus developing systems. *J. Atmos. Sci.*, **38**, 1132–1151, https://doi.org/10.1175/1520-0469(1981)038<1132:OAOTCF>2.0.CO;2.

Moore, B. J., L. F. Bosart, D. Keyser, and M. L. Jurewicz, 2013: Synoptic-scale environments of predecessor rain events occurring east of the Rocky Mountains in association with Atlantic Basin tropical cyclones. *Mon. Wea. Rev.*, **141**(3), 1022–1047, https://doi.org/10.1175/MWR-D-12-00178.1.

Nava, O. A., 2016: Influence of cloud-radiative processes on predecessor rain events. PhD dissertation, University of California.

Ninomiya, K., 1984: Characteristics of Baiu front as a predominant subtropical front in the summer northern hemisphere. *J. Meteor. Soc. Japan. Ser. II*, **62**, 880–894, https://doi.org/10.2151/jmsj1965.62.6_880.

Palmen, E., and C. W. Newton, 1969: *Atmospheric Circulation Systems*. Academic Press, 606 pp.

Petterssen, S., 1936: Contribution to the theory of frontogenesis. *Geofys. Publ.*, **11**(6), 1–27. https://urn.nb.no/URN:NBN:no-nb_digibok_2018020248114. Petterssen, S., 1956: *Weather Analysis and Forecasting. Vol. 1*. 2nd ed. McGraw-Hill, 428 pp.

Pfeffer, R. L., and M. Challa, 1981: A numerical study of the role of eddy fluxes of momentum in the development of Atlantic hurricanes. *J. Atmos. Sci.*, **38**, 2393–2398, https://doi.org/10.1175/1520-0469(1981)038<2393:ANSOTR>2.0.CO;2.

Pierce, C. H., 1939: The meteorological history of the New England hurricane of Sept. 21, 1938. *Mon. Wea. Rev.*, **67**(8), 237–285, https://doi.org/10.1175/1520-0493(1939)67<237:TMHOTN>2.0.CO;2.

Schumacher, R. S., T. J. Galarneau, and L. F. Bosart, 2011: Distant effects of a recurving tropical cyclone on rainfall in a midlatitude convective system: A high-impact predecessor rain event. *Mon. Wea. Rev.*, **139**(2), 650–667, https://doi.org/10.1175/2010MWR3453.1.

Shen, Y., Y. Pan, J. J. Yu, P. Zhao, and Z. J. Zhou, 2013: Quality assessment of hourly merged precipitation product over China. *Transactions of Atmospheric Sciences*, **36**(1), 37–46, https://doi.org/10.3969/j.issn.1674-7097.2013.01.005. (in Chinese with English abstract)

Sun, R., H. Yuan, X. Liu, X. Jiang, 2016: Evaluation and hydrological application of satellite-based precipitation datasets in driving hydrological models over the Huifa river basin in Northeast China. *J. Hydrol.*, **536**, 302–319, https://doi.org/10.1016/j.jhydrol.2016.02.054.

Tao, S. Y., 1980: *Heavy Rainfall in China*. Science Press, 130–131. (in Chinese). https://book.sciencereading.cn/shop/book/Booksimple/show.do?id=B7F3283B6765943A8907AB141430F0E31000.

Uccellini, L. W., and D. R. Johnson, 1979: The coupling of upper and lower tropospheric jet streaks and implications for the development of severe convective storms. *Mon. Wea. Rev.*, **107**(6), 682–703,

Van Nguyen, H., and Y. L. Chen, 2011: High-resolution initialization and simulations of Typhoon Morakot (2009). *Mon. Wea. Rev.*, **139**(5), 1463–1491, https://doi.org/10.1175/2011MWR3505.1.

Wang, D. H., X. F. Li, and W. K. Tao, 2010: Cloud radiative effects on responses of rainfall to large-scale forcing during a landfall of severe tropical storm Bilis (2006). *Atmospheric Research*, **98**(2–4), 512–525, https://doi.org/10.1016/j.atmosres.2010.08.020.

Wang, D. H., X. F. Li, W. K. Tao, Y. Liu, and H. G. Zhou, 2009a: Torrential rainfall processes associated with a landfall of severe tropical storm Bilis (2006): A two-dimensional cloud-resolving modeling study. *Atmospheric Research*, **91**(1), 94–104, https://doi.org/10.1016/j.atmosres.2008.07.005.

Wang, D. H., X. F. Li, W. K. Tao, and Y. Wang, 2009b: Effects of vertical wind shear on convective development during a landfall of severe tropical storm Bilis (2006). *Atmospheric Research*, **94**(2), 270–275, https://doi.org/10.1016/j.atmosres.2009.06.004.

Wang, Y., Y. Wang, H. Fudeyasu, 2009c: The role of Typhoon Songda (2004) in producing distantly located heavy rainfall in Japan. *Monthly Weather Review*, **137**(11), 3699–3716,

https://doi.org/10.1175/2009MWR2933.1.

Xie, P. P., R. Joyce, and S. Wu, 2013: A 15-year high-resolution gauge-satellite merged analysis of precipitation. Preprints, 27th Conf. on Hydrology, Austin, TX, Amer. Meteor. Soc..

Xie, P. P., R. Joyce, S. R. Wu, S. H. Yoo, Y. Yarosh, F. Y. Sun, and R. Lin, 2017: Reprocessed, bias-corrected CMORPH global high-resolution precipitation estimates from 1998. *Journal of Hydrometeorology*, **18**(6), 1617–1641, https://doi.org/10.1175/JHM-D-16-0168.1.

Xiong, Z., S. Y. Wang, Z. M. Zeng, and C. B. Fu, 2003: Analysis of simulated heavy rain over the Yangtze River valley during 11–30 June 1998 using RIEMS. *Adv. Atmos. Sci.*, **20**(5), 815–824, https://doi.org/10.1007/bf02915407.

Xu, H. X., 2015: A numerical study on impact of Taiwan Island surface heat flux on super Typhoon Haitang (2005). *Advances in Meteorology*, **2015**, 710348, https://doi.org/10.1155/2015/710348.

Xu, H. Y., G. Q. Zhai, and X. F. Li, 2017: Precipitation efficiency and water budget of Typhoon Fitow (2013): A particle trajectory study. *Journal of Hydrometeorology*, **18**(9), 2331–2354, https://doi.org/10.1175/JHM-D-16-0273.1.

Xu, H. Y., D. R. Zhang, and X. F. Li, 2021: The impacts of microphysics and terminal velocities of graupel/hail on the rainfall of Typhoon Fitow (2013) as seen from the WRF model simulations with several microphysics schemes. *J. Geophys. Res.: Atmos.*, **126**, e2020JD033940, https://doi.org/10.1029/2020JD033940.

Xu, H. X., Y. H. Duan, and X. D. Xu, 2022: Indirect effects of binary typhoons on an extreme rainfall event in Henan province, China from 19 to 21 July 2021: 1. Ensemble-based analysis. *J. Geophys. Res.: Atmos.*, **127**, e2021JD036265, https://doi.org/10.1029/2021JD036265.

Yang, S., K. Deng, M. Ting, and C. Hu, 2015: Advances in research on atmospheric energy propagation and the interactions between different latitudes. *Journal of Meteorological Research*, **29**(6), 859–883, https://doi.org/10.1007/s13351-015-5088-5.

Ying, M., W. Zhang, H. Yu, X. Q. Lu, J. X. Feng, Y. X. Fan, Y. T. Zhu, and D. Q. Chen, 2014: An overview of the China Meteorological Administration tropical cyclone database. *J. Atmos. Oceanic Technol.*, **31**, 287–301, https://doi.org/10.1175/JTECH-D-12-00119.1.

Yin, J. F., H. D. Gu, X. D. Liang, M. Yu, J. S. Sun, Y. X. Xie, F. Li, and C. Wu, 2022: A possible dynamic mechanism for rapid production of the extreme hourly rainfall in Zhengzhou City on 20 July 2021. *Journal of Meteorological Research*, **36**, 6–25, https://doi.org/10.1007/s13351-022-1166-7.

Yuan, J. P., D. Zhao, R. W. Yang, and H. F. Yang, 2018: Predecessor rain events over China's low-latitude highlands associated with Bay of Bengal tropical cyclones. *Climate Dyn.*, **50**(3–4), 825–843, https://doi.org/10.1007/s00382-017-3643-8.

Zhang, Q. H., K. H. Lau, H. Q. Wang, and S. J. Chen, 2000: Numerical simulation on mesoscale convective system along Mei-Yu front in Southern China. *Chinese Science Bulletin*, **45**(22), 2093–2096, https://doi.org/10.1007/BF03183534.

Zhang, S. L., S. Y. Tao, Q. Y. Zhang, and J. Wei, 2002: Large and meso-α scale characteristics of intense rainfall in the mid - and lower reaches of the Yangtze River. *Chinese Science Bulletin*, **47**(9), 779–786, https://doi.org/10.1360/02tb9176.

Zhao, Y., X. D. Xu, B. Chen, and Y. J. Wang, 2016: The upstream "strong signals" of the water vapor transport over the Tibetan Plateau during a heavy rainfall event in the Yangtze River Basin. *Adv. Atmos. Sci.*, **33**(12), 1343–1350, https://doi.org/10.1007/s00376-016-6118-7.

Zhao, P., J. Sun, and X. J. Zhou, 2003: Mechanism of formation of low level jets in the South China Sea during spring and summer of 1998. *Chinese Science Bulletin*, **48**(12), 1265–1270, https://doi.org/10.1007/BF03183949.

Zhao, P., R. H. Zhang, J. P. Liu, X. J. Zhou, and J. H. He, 2007: Onset of southwesterly wind over eastern China and associated atmospheric circulation and rainfall. *Climate Dyn.*, **28**(7–8), 797–811, https://doi.org/10.1007/s00382-006-0212-y.